Internal structures and dating of non-sulphide Zn deposits using rock magnetism: Insights from the Moroccan High-Atlas

Nicolas CHARLES[1,*], Flavien CHOULET[2], Stanislas SIZARET[3], Yan CHEN[3], Luc BARBANSON[3], Aomar ENNACIRI[4], Lakhlifi BADRA[5], Yannick BRANQUET[3].

1: Bureau de Recherches Géologiques et Minières (BRGM-French Geological Survey), Orléans, France
2: Université de Franche-Comté, UMR-CNRS 6249 Chrono-Environnement, Besançon, France
3: Institut des Sciences de la Terre d'Orléans, UMR 7327-CNRS/Université d'Orléans/BRGM, Orléans, France
4: Groupe Managem, Casablanca, Morocco
5: Université Moulay Ismaïl, Meknès, Morocco

Abstract

The renewal of interest in Zn-Pb non-sulphide ores has been induced by mineral processing improvement and leads to new exploration and mining projects in the world. Although the mineralogy is often precisely known, and despite several studies linking ore deposition to regional tectonics, absolute dating of non-sulphide stages is rare and structure of ore bodies was largely disregarded. Geochronological data from non-sulphide ores are essential to timely constrain alteration episodes and to insert supergene ore genesis in the climate and tectonic evolution of the metallogenic province. The access to internal organisation of ore could reveal post-mineralization episodes related to supergene evolution. Thus, a rock magnetism study combining Anisotropy of Magnetic Susceptibility (AMS) and palaeomagnetism was performed on four non-sulphide deposits from the Moroccan High-Atlas. AMS generally shows similar horizontal magnetic fabrics for ores and the clayey and carbonaceous internal sediments filling karstic cavities. The palaeomagnetic directions of ores and internal sediments are compatible and the calculated poles are consistent with the last 30

Ma of the Africa Apparent Polar Wander Path, with an upper age at 0.78 Ma. The proposed three-step scenario is placed within the evolution of the Moroccan High-Atlas belt. Deposition of primary sulphides is contemporaneous with opening of the Tethyan and Atlantic oceans. During the Tertiary, intracontinental deformation gave rise to the High-Atlas fold-and-thrust belt and to regional uplift. Finally, Zn-Pb sulphides, hosted in carbonates experienced oxidation under an arid climate to form karst-related Zn-Pb non-sulphide ores. These promising results pave the way for an efficient method to constrain the internal fabrics and age of Zn supergene deposits.

Key-words: non-sulphide Zn deposit, AMS, palaeomagnetism, dating, High-Atlas, Morocco.

*Corresponding author: n.charles@brgm.fr

1. Introduction

Non-sulphide zinc ores, also called “calamines” or “zinc oxides” were the main sources of zinc metal until the end of the nineteenth century (e.g. Large 2001; Boni et al. 2003; Hitzman et al. 2003). New processing technologies, such as hydrometallurgical acid-leaching, solvent extraction (SX) and electro-winning techniques (Cole and Sole 2002; Gnoinski 2007; Hosseini 2008), recently lead to a regain of interest in non-sulphide Zn-Pb ores with exploration and mining projects in Iran (Daliran et al. 2009; 2013), Namibia (Borg et al. 2003), Zambia (Terraciano 2008), Turkey (Santoro et al. 2013) and Peru (Boni et al. 2009). In non-sulphide Zn ores, zinc occurs as a major component of carbonates (smithsonite), silicates (willemite), hydrated minerals (Zn-clays, hemimorphite, hydrozincite) and minor phases listed in Hitzman et al. (2003). Based on physico-chemical conditions for

mineral occurrence, hypogene and supergene deposits have been distinguished (Heyl and Bozion 1962; Large 2001; Hitzman et al. 2003). Only supergene deposits will be discussed in this article.

During the last decade, many efforts have been made on understanding metallogeny of non-sulphide zinc deposits. Research has focused on describing the different zinc-bearing minerals (e.g. Borg et al. 2003; Boni et al. 2009; Daliran et al. 2009) and identifying the physico-chemical conditions they were formed (e.g. Boni et al. 2003; Reichert and Borg 2008; Choulet et al. 2014). Although the succession of mineral assemblages is often known in detail, absolute dating of non-sulphide stages is rare and limited to particular geochronometers such as Rb/Sr on willemite or clay (Schneider et al. 2008), U/Th-He on zinc vanadate (Boni et al. 2007) or Ar/Ar on zinc-lead manganese oxide (Groves et al. 2003). Obtaining geochronological data from non-sulphide mineralogical assemblage are essential to timely constrain oxidation episodes and to insert supergene ore genesis in the climate and tectonic evolution of the metallogenic province. In addition, despite several studies linking ore deposition to regional tectonics (Borg 2003; 2009), the structure of ore bodies was largely disregarded, as a consequence of the intricate supergene processes involved in karst-related deposits, where multiple weathering episodes and evolution of the hydrodynamics have contributed to successive chemical and mechanical reworking, respectively (Boni et al. 2003). Therefore, macroscopic and microscopic observations are often not sufficient to decipher the ore internal structure. To image these fabrics, it is possible to recourse to magnetic properties of minerals and especially to anisotropy of the magnetic susceptibility (AMS). This tool may provide information on the internal organisation of ore and can be used to reveal post-mineralization episodes related to supergene evolution (e.g. Essalhi et al. 2009). When geochronometer minerals are absent, the approach of palaeomagnetism can be also useful to indirectly constrain the age of mineralization. These methods have been successfully applied

77 to various types of deposits like VMS gossan (Essalhi et al. 2011), MVT (Symons et al. 1996;
78 2002), and iron laterites (Théveniaut and Freyssinet 1999; 2002; Théveniaut et al. 2007;
79 Ricordel-Prognon et al. 2010). Boni et al. (2005) attempted dating of non-sulphide Zn-Pb ores
80 of SW Sardinia (Italy) by palaeomagnetism. Despite scarce sampling and non-conclusive
81 results, the authors suggested that this method can be effective to constrain the timing of
82 oxidation in supergene-enriched ores, representing an interesting methodological challenge
83 with multiple possible targets throughout the world.

84 This contribution aims at showing that rock magnetism properties may be used to
85 constrain age and geometry in supergene ore deposits, with the example of the Moroccan zinc
86 non-sulphide deposits. The Moroccan High Atlas is an intracontinental Cenozoic belt that
87 exposes numerous supergene Zn non-sulphide deposits hosted in the Lower Jurassic
88 limestone (**Figure 1**). Choulet et al. (2014) studied the mineralogical assemblage of six
89 deposits and identified a direct replacement of Zn-Pb sulphides by carbonates and silicates,
90 accompanied by precipitation of Zn non-sulphide minerals in cavities with internal karstic
91 sedimentary filling. Based on field observations, they proposed that formation of the non-
92 sulphide ore is coeval with Atlas deformation and uplift during the Cenozoic. Therefore this
93 area represents a good target to use palaeomagnetism to timely constrain the supergene
94 oxidation episodes. We have selected four localities (Aït Labbès, Toulal, Beni Tajite and
95 Tadaghast; **Figure 1**) and collected samples from both veins of non-sulphide Zn ore and
96 cavities filled by internal karstic sediments. After a careful study of the mineralogy to identify
97 the magnetic carriers, we present AMS and palaeomagnetism results that allow us to discuss
98 the internal structure of the mineralized body and its age in the general framework of the
99 Atlas tectonic and climate evolution.

100

101 **2. Geological and metallogenetic setting**

2.1. The Moroccan High-Atlas

The Atlas Mountains is an intracontinental orogen, WSW-ENE trending mountain belts, extending from Morocco to Tunisia (e.g. Frizon de Lamotte et al. 2009 and references therein; **Figure 1a**). The Moroccan High-Atlas is composed of Mesozoic to Cenozoic sedimentary rocks overlying on a Precambrian to Palaeozoic basement (**Figures 1b and 1c**), deformed during the Variscan orogeny (Mattauer et al. 1977; Piqué and Michard 1989). According to Laville and Piqué (1991), inheritance of Palaeozoic structures largely constrains the geometry of the Mesozoic rifting episode related to the opening of the Tethys and the Atlantic Ocean. The sedimentary pile comprises from bottom to the top: 1) Triassic detrital rocks, evaporites (du Dresnay 1988; Piqué 1994) associated with mafic volcanics lava, 2) Lower to Middle Jurassic marl, limestone and calcareous turbidite, and 3) upper Middle Jurassic continental red beds (Charrière et al. 2005) with contemporaneous magmatism (Brechbühler et al. 1988; Laville and Piqué 1992). Sedimentation resumed with Cretaceous red sandstone and limestone deposits. The Late Cretaceous carbonate platform marks a short but major Late Cenomanian-Turonian transgression event (Haddoumi et al. 2008), since continental sedimentation is recorded again at the end of Cretaceous, during the Palaeocene (Charrière et al. 2009) and until the mid-Eocene (Herbig and Trappe 1994).

Presently, the Moroccan High-Atlas exhibits a fold-and-thrust bulk architecture that results from inversion tectonics of the former Mesozoic extensional basins, controlled by NE-SW trending normal faults (Laville et al. 2004; Frizon de Lamotte et al. 2008). The NE-SW strike of the faults is slightly oblique to the general ENE-WSW trend of the belt (**Figure 1a**). Lower to Middle Jurassic strata are found in the wide and open synclines, while anticlines are comparatively narrow and are underlined by thick Lower Jurassic limestone ridges (**Figure**

1c). Locally, the anticline hinges are affected by thrusting, exposing the underlying Triassic strata that form the décollement layer. The formation of the intracontinental belt in the Moroccan High-Atlas (Mattauer et al. 1977) has been facilitated by the inherited crustal weaknesses due to Mesozoic rifting. Although the chronology of faulting and uplift is still disputed, inversion tectonics of the Triassic to Jurassic normal faults occurred between Eocene and Quaternary, with alternation of quiet and active periods of uplift (Frizon de Lamotte et al. 2009). While compression chiefly occurs at the Lutetian-Bartonian transition (ca. 40 Ma), a secondary Pleistocene episode has caused the present topography of the range.

The Lower Jurassic carbonate massif of the Moroccan High Atlas has experienced intense karstification driven by 1) the tectonic structures relative to Tertiary tectonics, and 2) the lithology, with a preferred development of karst network in reef limestone and dolostone (Couvreur, 1978). Several episodes of karst development have been recorded in the literature: 1) an early stage (Lower Jurassic) coeval with sulphide deposition is recorded at Beni Tajite deposit (Choulet et al. 2014), a Cretaceous event during a major emersion phase (Subra, 1980), post-Eocene to Mio-Pliocene episodes related to the Atlas tectonics and exhumation of the Jurassic rocks (Bouchaou, 1988), and Pliocene to Quaternary evolution (Nicod, 1997) driven by the reactivation of Atlas faults.

2.2. Non-sulphide Zn-Pb deposits of Moroccan High-Atlas

The numerous Zn-Pb ore deposits in Northern Africa belong to the Zn-Pb province of the circum-Mediterranean Sea and Alpine Europe (Rouvier et al. 1985), a wide area of economic interest for the extraction of base metals (Emberger 1969; Popov 1968; Decrée et al. 2008; 2010; Bruyère et al. 2010; Jemmali et al. 2011). In the Moroccan High-Atlas, Zn-Pb ore deposits occur throughout the belt (**Figure 1b**). Two main metallogenic periods have been

recognized for Zn-Pb sulphide ore deposition (Mouguina 2004): (1) the Lower Jurassic period, with stratabound lenses of Zn-Pb-Fe sulphides considered as syngenetic (Agard and du Dresnay 1965; Emberger 1965; Bazin 1968; Auajjar and Boulègue 1999); (2) the Middle Jurassic (i.e. Dogger) period, characterized by Cu-Ni and Zn-Pb ore deposits spatially and temporally associated to mafic magmas, and to reactivated faults (Caïa 1968; Chèvremont 1975).

In the Moroccan High-Atlas, Zn-Pb mineralization often consists of non-sulphide zinc ores, locally called "calamines" (Ovtracht 1978), which are considered to result from the supergene alteration of a primary carbonate-hosted sulphide protore (Agard and du Dresnay 1965; Bazin 1968; Leblanc 1968; Mouguina 2004). The origin of primary sulphides (Sedex or MVT types) is not clearly established yet and is beyond the scope of this paper. Based on field and mineralogical studies of six non-sulphide Zn-Pb deposits, Choulet et al. (2014) recently published a new model to explain the formation of Moroccan High-Atlas non-sulphide ore deposits. They recognized two superimposed stages of weathering, following the formation of the protore sulphides (themselves more or less coeval with deposition of Lower Jurassic host limestone):

- (1) early supergene weathering with formation of Zn-Pb carbonates and iron oxi-hydroxides,

- (2) late supergene weathering with deposition of Zn-carbonates, Zn-silicates and hydrated phases.

The proposed scenario falls within the tectonic evolution of the Moroccan High Atlas belt. Deposition of primary sulphides is contemporaneous with opening of the Tethyan and Atlantic oceans. During the Tertiary, intracontinental deformation has given rise to the High Atlas fold-and- thrust belt and to regional uplift. As a result, Zn–Pb sulphides, hosted in carbonates experienced oxidation under an arid climate to form karst-related Zn–Pb non-

177 sulphide ore bodies. Our good understanding of processes involved and the well-established
178 chronology allow us to study, rock magnetism to constrain the ore body structure and its
179 formation age by means of magnetic fabrics and palaeomagnetism, respectively. Despite this
180 complex weathering evolution, iron-bearing phases representing the main magnetic carriers,
181 are formed during the early supergene event and not reworked by the late one, apparently
182 preventing remagnetization.
183
184 2.3. The Tadaghast, Aït Labbès, Toulal and Beni Tajite ore deposits
185
186 In this study, four occurrences and deposits have been investigated: Tadaghast, Aït
187 Labbès, Toulal and Beni Tajite (**Figure 1b**). The geological setting has been extensively
188 studied by Choulet et al. (2014). Only a brief outline of macroscopic and microscopic
189 observations is provided here (Figures 2 and 3), and the reader can refer to Choulet et al.
190 (2014) and references therein for a more detailed description.
191 In the field, non-sulphide Zn-Pb deposits are often associated to tightly faulted
192 anticlines (**Figure 2a**), except for the tabular series that hosts the Beni Tajite ore deposit
193 (Agard and du Dresnay 1965). Non-sulphide ores are always hosted in Lower Jurassic
194 limestone formed in a reefal or para-reefal environment commonly close to the transition
195 from the platform to the deep sea (du Dresnay 1979; Leblanc 1968). Mineralized system is
196 associated to a karst-related network formed after tectonic features and exposing dissolution
197 cavities in the limestone, as well exemplified at Toulal and Aït Labbès sites (**Figures 2b, 2c**
198 **and 2d**).
199 The protore mainly consists of stratabound lenses of primary sulphides (galena,
200 sphalerite and pyrite; **Figure 3a**) and massive white calcite. Superimposed supergene
201 oxidation includes the formation of non-sulphide Zn-Pb minerals and iron oxi-hydroxides

(e.g. smithsonite, hemimorphite, hydrozincite, goethite, hematite; **Figures 2e and 2g**). Two successive types of non-sulphide ores have been observed all over the studied sites (Choulet et al. 2014; **Figures 2h and 2i**):

- a red ore (locally called red calamine) composed of the iron oxi-hydroxides-smithsonite association (**Figures 2h, 3b and 3c**); in all samples dissolved pyrite are replaced by zoned goethite and hematite (Choulet et al. 2014).

- a "grey to white ore" (locally called grey or white calamine) superimposed on the red type or precipitated in karst cavities with limited metal transport (**Figures 2i and 3d**). It is worth to notice that no iron oxi-hydroxides are involved in this second stage.

Besides, the development of the karst network within limestone host-rocks implies internal sedimentation, as evidenced by horizontally bedding within up to 10 meters scale cavities (**Figure 2f**). Locally, the horizontal bedding is disturbed due to either sedimentary processes or post-deposition tectonics. Although interference between karst formation and supergene evolution of ore may occur, internal sediments are usually Zn-poor (grading 4-5 ZnO wt.%, Choulet et al., 2014), and mainly made up of marl and calcareous shale including clasts of calamine and iron (hydr-)oxides (**Figures 3e and 3f**). Laminated internal sediments display micrometric to centimetric alternations of banded calcite and matrix-supported beds including detrital residual clays and a mix of carbonate and iron oxides coeval with the karst development (**Figure 3e**). Alternatively, clast-supported sediments present sub-rounded fragments of iron oxides and calcite. These clasts are cemented by secondary massive or drusy calcite (**Figure 3f**). Finally, a synoptic paragenetic sequence can be proposed for all the studied deposits as shown in **Figure 3g**.

3. Methods and sampling

227 3.1. Sampling strategy

228

229 Using a portable gasoline drill, a total of 157 cores has been collected from non-
230 sulphide Zn ore (98 cores), internal sediment (39 cores) and host Lower Jurassic limestone
231 (20 cores) in four localities (**Figure 1b**): Aït Labbès (AL), Toulal (T), Beni Tajite (BT) and
232 Tadaghast (TA). At Aït Labbès, 51 cores (38 of non-sulphide Zn ore, 9 of internal sediment
233 and 4 of host limestone) were sampled in a bunch of N60°-trending cavities at 3 sites (i.e.
234 AL1, AL2 and AL3; **Figures 4a, 4b and 4c**). At the Toulal prospect, 47 cores (15 of non-
235 sulphide Zn ore, 22 of internal sediment and 10 of host limestone) were collected at 3 sites
236 (i.e. T1, T2 and T3; **Figures 4d, 4e and 4f**). At Beni Tajite, 30 cores were drilled in grey non-
237 sulphide Zn ore (i.e. BT1 and BT2; **Figure 4g**). Finally, 29 cores (15 of non-sulphide Zn ore,
238 8 of internal sediment and 6 of host limestone) were collected at Tadaghast, in the currently
239 exploited galleries with two sites corresponding to E-W sub-vertical and stratabound veins
240 (TA1 and TA2, respectively; **Figures 4h and 4i**). Cores have been oriented with both
241 magnetic and sun compasses, when it was possible, to correct the local magnetic field
242 anomalies. The average difference between magnetic and solar declinations is about 5.8°. In
243 additions, two blocks oriented on field have been collected at Toulal (T3) and Tadaghast
244 (TA6) and further drilled in lab. Then, cores were cut into standard specimens of 22 mm in
245 length and 25 mm in diameter for both AMS and palaeomagnetic measurements.

246

247 3.2. Methods and analytical procedure

248

249 *3.2.1. Anisotropy of Magnetic Susceptibility (AMS)*

250

Magnetic susceptibility (K) is defined by K=M/H where M is the induced magnetization of the material and H, the inducing magnetic field (see Rochette et al. 1992 for details). The susceptibility is described as a symmetric second rank tensor, which can be depicted by an ellipsoid defined by three orthogonally oriented axes: K_1, K_2 and K_3 (with $K_1 \geq K_2 \geq K_3$). K_1 and K_3 are considered to be the magnetic lineation and the pole of the magnetic foliation, respectively. Thus, the Anisotropy of Magnetic Susceptibility (AMS) is the property of a material whereby a given magnetic field applied in different directions produce variable intensities of induced magnetization. A number of parameters can be calculated to characterize the AMS ellipsoid, but the most widely used are the mean magnetic susceptibility (K_m), the corrected anisotropy degree (P_J), and the shape parameter (T) (Tarling and Hrouda 1993). In the case of low susceptibility, these parameters and especially the P_J values should be used with caution, as it has not been corrected from the diamagnetic component (not measured in this study). The AMS is a physical property of rocks that define the magnetic fabric and is used for characterizing internal rock textures and structures (e.g. Hrouda 1982; Sizaret et al. 2003; Charles et al. 2009; 2012; Essalhi et al. 2009).

3.2.2. Palaeomagnetism

Palaeomagnetism relies on the study of the magnetic remanence involved by ferromagnetic *s.l.* minerals present in the rocks. During sediment deposition, or syn-diagenetic precipitation, these minerals may record the Earth magnetic field that can be preserved through time and be used for indirect age constraints (e.g. Van der Voo 1993). Dating ore deposition through palaeomagnetism, especially stratabound, disseminated and massive sulphide ore deposits has beneficiated of major advances since last two decades (e.g. Symons et al. 1996; 2002; Symons and Stratakos 2000; Leach et al. 2001; Bradley and Leach

2003; Pannalal et al. 2008). Palaeomagnetism can be also used to establish the timing of weathering, with characteristic example of laterite profiles or gossans (Théveniaut and Freyssinet 1999; 2002; Théveniaut et al. 2007; Ricordel 2007; Ricordel-Prognon et al. 2010; Essalhi et al. 2011). Hence, the absence of time constraints for non-sulphide Zn-Pb deposits of Moroccan High-Atlas could be overcome using palaeomagnetism coupled with field observations and a detailed mineralogical study (Choulet et al. 2014).

3.2.3. Technical procedure

Prior to carry out the AMS and palaeomagnetic studies, magnetic mineralogy has been investigated by four techniques: (1) X-ray diffraction (INEL XRM3000 diffractometer in transmission mode coupled to an INEL CPS 120 curved position sensitive detector), (2) thermomagnetic measurements (AGICO CS3 coupled with AGICO KLY3-S Kappabridge apparatus), (3) Isothermal Remanent Magnetization (IRM; AGICO JR5-A spinner magnetometer coupled with ASC Scientific IM-10-30) and (4) bulk magnetic susceptibility (AGICO KLY3-S Kappabridge apparatus). We have further measured the Anisotropy of Magnetic Susceptibility using AGICO KLY-3S Kappabridge apparatus and the average orientation of the three principal ellipsoidal axes of AMS for groups of samples was computed with ANISOFT software using Jelinek's statistics (Jelinek 1981). Both thermal and Alternative Field (AF) demagnetizations have been carried out by laboratory-built furnace and AGICO LDA-3 demagnetizer, respectively. Step heating includes an average of ten steps between natural remanent magnetization (NRM) and 680°C. The magnetic remanence was measured using AGICO JR5-A spinner magnetometer to remove recent viscous remanent magnetization components from the magnetic remanence of specimens. The directions of the magnetic remanence were isolated by principal component analysis (Kirchvink 1980) and

mean directions were computed by spherical statistics (Fisher 1953) using palaeomagnetic software packages of Cogné (2003) and R. Enkin (unpublished). All measurements were performed at Institut des Sciences de la Terre d'Orléans (ISTO).

4. Results

4.1. Magnetic mineralogy of non-sulphide Zn-Pb deposits and internal karstic sediment

X-ray diffraction pattern reveals that red ore is composed of goethite, calcite and smithsonite (**Figures 5a and 5b**), whereas grey calamine only includes smithsonite (**Figure 5c**). For internal sediments, goethite, calcite and quartz have been identified (**Figure 5d**), and the large bulge at small θ values attests for a significant clay minerals component. These results are in accordance with field and microscopic observations (**Figures 2 and 3**).

Bulk magnetic susceptibility intervals for each lithology are plotted in **Figure 6**. The majority of ore samples present magnetic susceptibilities lower than 200.10^{-6} SI and up to 800.10^{-6} SI suggesting the contribution of ferromagnetic *s.l.* minerals. The magnetic susceptibilities of internal sediment and host limestone samples are weakly positive (below 100.10^{-6}SI), suggesting that both rock types include paramagnetic minerals, with a small amount of ferromagnetic *s.l.* minerals. In addition, several ore samples (mainly grey ore) display negative values of bulk magnetic susceptibility, suggesting the dominance of diamagnetic minerals, like iron free carbonate.

Isothermal remanent magnetization (IRM) was carried out on 11 representative samples (ores and internal sediments), and results are presented in **Figure 7**. For this technique, samples are magnetized in an increasing direct magnetic field and the resulting IRM saturation pattern is typical of the different ferromagnetic *s.l.* minerals. The red ore and

internal sediments samples from Aït Labbès, Toulal and Tadaghast show similar patterns (**Figures 7a, 7b and 7d**). Samples exhibit a first rapid increase of the induced field at weaker applied fields leading to consider the presence of low-coercive minerals (e.g. magnetite). Then, a lack of magnetic saturation at an applied magnetic field up to 1.4 T is observed, which is typical of high-coercive minerals, such as goethite and/or hematite. For the grey ore of Beni Tajite (**Figure 7c**), the saturation below 150 mT indicates the occurrence of low-coercive minerals (e.g. magnetite). The magnitude of remanence confirms the low concentration of magnetic minerals.

Thermal monitoring of the magnetic remanence and the magnetic susceptibility (Curie temperature evaluation) are presented in **Figure 8**. For the red ore collected at Aït Labbès, Toulal and Tadaghast, thermomagnetic curves (**Figures 8a, 8b and 8c**) present two or three drops of the magnetic remanence at about 100-120°C, 300-350°C (only for samples AL2-3B and T2-11) and 580°C, corresponding to goethite, maghemite (titanomaghemite) and magnetite Curie temperatures, respectively. These observations are partially confirmed by thermal magnetic measurements with magnetic susceptibility dropping at around 300-350°C and 580°C (**Figure 8d)**. The presence of hematite, observed under microscope (Choulet et al. 2014) is probable, as magnetic remanence and susceptibility values continue to slightly drop beyond 580°C (**Figures 8a to 8d**). For internal sediments, the evolution of the magnetic remanence with temperature is the same for each locality, with two drops at around 100-150°C and 580°C (**Figures 8e, 8f and 8g**), in accordance with the presence of goethite and magnetite. Minor hematite is also suspected by the slight drop at 580°C (especially for sample T1-17). This observation partially coincides with thermal magnetic measurements as magnetic susceptibility dropping up to 580°C is due to the magnetite Curie temperature (**Figure 8h**). As for the red ore, hematite is probably present owing to the pattern of magnetic remanence and susceptibility curves above 580°C (**Figure 8f**).

351

352 4.2. Magnetic fabric study (AMS)

353

354 At Aït Labbès, the AMS pattern is highly heterogeneous for red ore samples, with
355 variable directions of the principal axes and broad error ellipses (**Figure 9a**). Nevertheless,
356 magnetic foliation appears to be relatively steep and roughly parallel to the azimuth of the
357 karst cavity (~N50°). For internal sediments, the magnetic foliation is well-defined and
358 horizontal, with a weakly constrained E-W lineation. In the host limestone, the lineation
359 presents a NW-SE trending and the magnetic foliation is slightly oblique, about 20°, a value
360 close to the dip of the bedding (**Figure 4a**). Both ore and internal sediment samples present
361 low values of the corrected anisotropy degree (P_J<1.01), without correlation with bulk
362 susceptibility, except for high values of susceptibility (**Figure 9a**). The coexistence of
363 positive and negative values of the shape parameter suggests that fabrics are both prolate and
364 oblate. Conversely, in the host limestone, P_J value is higher than 1.01, whilst bulk
365 susceptibility is very low; T value is positive and fabric is apparently oblate.

366 At Toulal, both ore and internal sediment samples present homogenous measurements
367 of the AMS principal axes directions, with a well-defined horizontal foliation and poorly
368 constrained WNW-ESE lineation (**Figure 9b**). As the host limestone is homogeneous for all
369 three sites, AMS measurements have been compiled into one stereogram (**Figure 9b**). The
370 fabric is quite well-defined and foliation exhibits a strong south-eastward dipping. In ore
371 samples, positive and negative T values are observed, as well as a strong variability of the P_J
372 parameter that is correlated with bulk susceptibility; the higher susceptibility is, the less the
373 corrected anisotropy degree is. Conversely, only oblate fabrics are observed for internal
374 sediments (positive T values), while P_J varies from 1 to 1.06 (**Figure 9b**).

375 The grey ore samples from Beni Tajite display a well-defined horizontal foliation and
376 NW-SE trending lineation (**Figure 10a**). The majority of T values are positive, suggesting a
377 dominantly oblate shape. Values of the corrected anisotropy degree are bracketed between
378 1.01 and 1.17, without correlation with bulk susceptibility.

379 As for Aït Labbès, the ore samples from Tadaghast display heterogeneous AMS
380 pattern, with variable directions of principal axes and large envelope error (**Figure 10b**). Both
381 positive and negative T values are observed, while P_J and bulk susceptibility values are
382 homogeneously weak. For the internal sediments, the fabrics are fairly defined with a
383 horizontal foliation and NW-SE lineation (**Figure 10b**). AMS parameters show P_J values
384 comprised between 1.02 and 1.04 with a bulk magnetic susceptibility yielding from 300 to
385 900.10^{-6} SI. Finally, the fabrics of the host limestone are quite well-defined with an steeply
386 inclined foliation (up to 70°). The P_J parameter varies from 1.01 to 1.04, while bulk
387 susceptibility (K_m) is very low (i.e. $<10^{-5}$ SI).

388

389 4.3. Palaeomagnetic results

390

391 The palaeomagnetic study was carried out on samples from Aït Labbès, Toulal and Tadaghast
392 localities. The average measured directions for specimen, sites and localities with the
393 corresponding statistical parameters are reported in **Table 2**.

394

395 *4.3.1. Aït Labbès deposit*

396

397 Stepwise demagnetization shows two principal magnetic components for red ore
398 samples distinguished at about 100-150°C (**Figures 11a and 11b**). The low-temperature
399 component (LTC) below 100-150°C is plunging downwards but its direction is scattered, not

consistent with the present-day geomagnetic field. The Characteristic Remanent Magnetization (ChRM) decays to the origin and is, either south to south-southwestwards and plunging upwards (**Figure 11a**) or north to northeastwards and plunging downwards (**Figure 11b**). Although the two opposed polarities are not strictly antipodal, and the reversal test (McFadden and McElhinny 1990) is negative (**Figure 11c**), the average direction of the two groups are similar within errors and a specimen-mean direction for red ore can be calculated at D = 11.1°, I = 42.8°, k = 31, α_{95} = 4.9°, with D and I as the respective declination and inclination of the remanent magnetization, k as the precision parameter and α_{95} as the radius of the 95% confidence circle (**Table 2**). After removing a scattered LTC, internal sediment specimens display a CHRM pointing toward to the origin (**Figure 11d**) with an unblocking temperature over 100-150°C. This component is chiefly north to north-northeastward and plunging upwards (**Figure 11d**). In addition, a south to southeastward and downward component is also observed from two specimens (**Figure 11e**). A specimen-mean direction from internal sediment can be calculated at D = 11.5°, I = 55.0°, k = 12.5, α_{95} = 19.7°, although these two groups with opposed polarities are not strictly antipodal (**Table 2**) and the reversal test is not positive.

4.3.2. Toulal prospect

At Toulal, all samples display a scattered LTC (northwestwards and dipping downwards). Red ore samples present a ChRM decaying to the origin, with unblocking temperatures at 100-150°C. This component is either northward and downward (**Figure 12a**), or south to south-southeastward and upward (**Figure 12b**). Despite a negative reversal test, the two groups of opposed polarities are antipodal, with mean directions similar within errors; a specimen-mean direction at D = 356.0°, I = 47.3°, k = 54.0, α_{95} = 7.1°, has been calculated

425 for the red ore samples at this locality (**Figure 12c and Table 2**). Identically, a north-
426 northwestward and dipping downward LTC is present in the internal sediments. The ChRM
427 (above 250°C) points to the origin, although demagnetization is not total for several hematite
428 rich specimens. Both northward and downward (**Figure 12d**), or south to south-
429 southwestward and upward (**Figure 12e**) directions have been observed for this component.
430 Despite scattering of individual specimens with reverse polarities, the two groups are
431 antipodal with positive reversal test, and we have calculated a specimen-mean direction at D
432 = 356.7°, I = 34.9°, k = 22.4, α_{95} = 9.4° for internal sediment (**Figure 12f and Table 2**).
433
434 *4.3.3. Tadaghast deposit*
435
436 Conversely at Tadaghast, both red ore and internal sediment samples present a
437 characteristic remanence magnetization (ChRM) decaying to the origin, after removing the
438 rare and scattered LTC. For ore specimens, the direction of this ChRM is south-southeastward
439 and plunging upwards (**Figure 13a**). Individual data are scattered (**Figure 13b**) and the
440 calculated specimen-mean at D = 154.4°, I = -57.2°, k = 18.7, α_{95} = 18.2° displays a high
441 statistical variability (**Table 2**). For internal sediment, the direction of ChRM is northeastward
442 and plunging downward (**Figure 13c**). Oppositely, data are grouped and at a specimen-mean
443 has been calculated at D = 20.3°, I = 34.1°, k = 216.1, α_{95} = 4.1° (**Figure 13d and Table 2**).
444
445 *4.3.4. Beni Tajite deposit*
446
447 Only 4 specimens out of 10 measured samples have produced a significant remanent
448 magnetization, probably due to a low concentration in ferromagnetic minerals. A ChRM
449 component has been isolated between 300°C and 600°C (**Figure 13e)**. As its direction is

relatively scattered and the number of specimen is small (**Figure 13f**), we cannot compute an average paleomagnetic direction and utilize it for dating this deposit.

5. Discussion

5.1. Internal structures of non-sulphide Zn-Pb deposits

Investigation of magnetic carriers has shown that internal sediment and red ore contain soft coercive minerals, magnetite and minor maghemite, and hard coercive minerals, like goethite with minor hematite (**Figure 7 and 8**). In grey ore and host limestone, the dominant magnetic carriers of susceptibility and remanence are often diamagnetic and paramagnetic minerals, although several samples may include a small amount of magnetite (**Figure 7**).

Iron oxi-hydroxides have been observed under optical and electronic microscopes in all deposits. Choulet et al. (2014) have established that both minerals pseudomorph pyrite depending on local pH conditions during early stage of supergene weathering. In addition, goethite may occur later in the succession to form thin bands that alternate with drusy smithsonite (**Figures 3b and 3c**) or to fill voids within geodes (**Figure 3d**). In all cases, goethite and hematite precipitate from iron-saturated solution, implying that the magnetic property, especially the magnetic remanence of the high temperature component partly carried by hematite is of chemical origin. In internal sediments, the iron oxi-hydroxides (hematite and goethite) have formed during diagenesis and thus imply a remanent magnetization of chemical origin too. However, the magnetic remanence is often totally removed at 580°C, so that chemical remanent magnetization is not the dominant one in both types of rocks. Our study of the magnetic mineralogy has also shown the ubiquitous occurrence of magnetite. In sedimentary rocks, magnetite is of detrital origin and its magnetic properties have been

475 acquired during particle deposition. Magnetite can also be formed during diagenesis and long-
476 lived burial (Aubourg et al. 2012), but such conditions (depth > 2km) have not been reached
477 in karst-related internal sediments as well as in red ore veins. Red ore is characterized by a
478 formation under an oxidizing environment, not compatible with the precipitation of
479 magnetite, especially under supergene conditions. Two hypotheses for the presence of
480 magnetite can be advanced: 1) recycling of detrital magnetite initially within the limestone,
481 but released after host rock dissolution, 2) occurrence of very small cavities of internal
482 sediments including detrital magnetite, which is frequently observed in ore samples (Choulet
483 et al. 2014). These results are partly consistent with the magnetic mineralogy investigated in
484 Sardinian non-sulphide ore deposits (Boni et al. 2005). Goethite and hematite represented the
485 main magnetic carriers and magnetite was not identified, as they did not collect samples
486 related to detrital processes, like karstic internal sediment.

487 According to AMS measurements, internal sediment samples present a sub-horizontal
488 magnetic foliation (**Figures 9 and 10**). A similar pattern is sometimes observed for ore
489 samples, although a local disturbance is also recorded. The data are more scattered in the host
490 limestone, but data are more distributed along a girdle that became horizontal after bedding
491 correction. This suggests that this pre-tilting magnetic fabric was initially horizontal and
492 could correspond to sedimentary deposition. Whatever the rock type, the magnetic lineation is
493 regularly NW-SE to W-E trending (**Figures 9 and 10**), which is consistent with the
494 orientation of the karstic cavities (**Figure 2**). AMS parameters and, especially, the corrected
495 anisotropy degree are generally low for ore and internal sediment (**Table 1**), suggesting that
496 post-deposition deformation is absent or not penetrative. The broad similarity of AMS
497 patterns between ore and internal sediment implies that same parameters control the
498 development of rock internal fabrics. As magnetic lineation parallels the trend of karst-related
499 cavities and magnetic foliation is horizontal whatever the morphology of the cavity, we

suggest that sedimentary processes within the cavity related to karst fluid dynamics driven by the regular network of first order fractures may control the internal structure of infilling material. In addition, the strong obliquity between horizontal magnetic foliation and the surrounding tectonic markers (faults, limestone bedding) argue for a post 40 Ma deposition of ores and internal sediments, after the main tectonic episode of Atlas (Frizon de Lamotte et al. 2009).

Locally, the individual specimens are scattered for a given site (e.g. AL1, AL2; **Figure 9a**), or define an oblique foliation (**Figure 10b**). This perturbation of the AMS signal may be explained by sedimentary recycling of ore and barren material during karst evolution (e.g. for Aït Labbès). In addition, the Atlas range results from multiple superimposed compressive events (Frizon de Lamotte et al. 2009), and these successive reactivations could explain the oblique fabric exemplified at Tadaghast. Hence it is highly probable that the karstic network has formed progressively throughout the Moroccan High Atlas, in relation with major compression events. Although most observations have revealed horizontal bedding in the cavity, early internal karstic sediment may have undergone polyphased tectonics and, as a consequence, the originally horizontal fabric has been tilted or removed during the recent uplift episodes.

5.2. Age(s) of Moroccan High-Atlas non-sulphide Zn-Pb deposits

At Aït Labbès and Toulal localities, we obtained a well-defined ChRM and chiefly antipodal directions that allow us to calculate mean site directions (**Figures 11 and 12**). The presence of two antipodal polarities for each rock type suggests that remanence is not due to a remagnetization and that our dataset averages the secular variations of the Earth magnetic field. This is also confirmed by our investigation of the magnetic mineralogy that suggests

525 magnetite and hematite as respective carriers of detrital and chemical remanence, acquired
526 during ore and sediment deposition or during late weathering. Although the primary origin of
527 magnetization cannot be surely assessed, the partial detrital origin for remanence may be
528 underlined by general horizontal bedding observed in the field and the shallow inclination of
529 AMS planar fabric. Although for some samples from Aït Labbès the magnetic fabric is not
530 horiziontal, this does not have significant influence on the scattering of remanent directions.
531 At Tadaghast, we obtained a well-constrained direction for internal sediment, but the
532 individual measurements for red ore are very scattered (**Figure 13**). For each lithology, a sole
533 polarity has been measured, so that the contemporaneity of ore and internal sediment cannot
534 be ascertained. Given our dataset, it is clearly impossible to advocate a primary chemical or
535 detrital origin of the remanence and the hypothesis of late weathering cannot be ruled out. In
536 addition, specimen-mean directions are not consistent between the two rock types and this can
537 be explained by: 1) false orientation of the specimen, because cores have been drilled at lab
538 from an oriented hand sample and 2) magnetic reworking, as AMS fabrics of red ore (**Figure**
539 **10**) are clearly oblique suggesting post-deposition tectonics or recent weathering. Despite a
540 relatively good consistency between Tadaghast internal sediments and other localities, we
541 cannot guarantee the reliability of these data, therefore we have excluded them from further
542 interpretation.
543 As specimen-mean directions calculated for red ore and internal sediment are
544 compatible for each locality (**Table 2**), we computed a specimen-mean direction including
545 these two lithologies at D = 11.1°, I = 44.8°, k = 24.2, α_{95} = 5.0° for Aït Labbès and at D =
546 356.4°, I = 40.3°, k = 26.5, α_{95} = 6.3° for Toulal (**Figure 14**). Furthermore, we have
547 calculated two palaeomagnetic poles: λ = 114.4°N, Φ = 78.6°E, dp/dm = 4.0°/6.4° for Aït
548 Labbès (32.38°N, -4.33°E) and λ = 196.7°N, Φ = 79.9°E, dp/dm = 4.2°/6.9° for Toulal
549 (32.30°N, -3.99°E). These two poles are statistically different within error. As several

550 measured specimens display reverse polarity, the upper age limit for localities corresponds to
551 the last magnetic reversal (Brunhes-Matuyama reversal) at ca. 0.78 Ma (Gradstein et al.
552 2004). **Figure 15** provides a comparison with the Apparent Polar Wander Path (APWP) of
553 Africa (Besse and Courtillot 2002). The Toulal pole is slightly isolated from the APWP but
554 the ellipse of confidence crosscuts the APWP individual poles at 10 Ma, 20 Ma and 30 Ma.
555 Hence, an age between 30 Ma and 10 Ma can be proposed for Toulal. This is consistent with
556 the horizontal AMS fabric that suggested post-tectonics deposition of red ore and internal
557 sediments after the main Atlas episode at ca. 40 Ma (Frizon de Lamotte et al. 2009).
558 Conversely, the palaeomagnetic pole calculated for Aït Labbès intersects the APWP and the
559 age is statistically between 60 Ma and 10 Ma. However, field observation suggested that red
560 ore and internal sediment do not predate the major compression episode at 40 Ma. Hence the
561 age of Aït Labbès pole is bracketed between 40 Ma and 10 Ma, and in detail, the pole plots
562 closer to the 40 Ma pole of APWP than to the younger one's (**Figure 15**). The apparent
563 diachronism between these two localities is in accordance with the differences in AMS
564 fabrics. The AMS pattern at Toulal shows a well-defined horizontal magnetic foliation and a
565 consistent magnetic lineation whose direction parallels the trend of the karst-related cavity.
566 Conversely, both magnetic foliation and lineation are badly constrained at Aït Labbès,
567 suggesting tectonic and sedimentary perturbations after ore and internal sediment deposition.
568 Palaeomagnetic data support the post-Atlasic age of supergene weathering inferred
569 from field observation (Choulet et al. 2014), but we could not improve this time interval,
570 similarly to Boni et al. (2003) for Sardinia non-sulphide ore deposits. The large age span of
571 our data can be explained by the limited dataset, although narrow ellipses of confidence for
572 pole attest for the reliability of data. Beyond statistically and sampling bias, the limited
573 movements of Africa during the last tens of million years (Besse and Courtillot 2002)
574 preclude a better constraint for recent episodes when age is based on palaeomagnetism.

575

576 5.3. Integration into the Moroccan High-Atlas geodynamic context

577

578 This study is the first attempt of dating the non-sulphide zinc deposits in the Moroccan
579 High Atlas. The obtained results are consistent with the timing of ore deposition proposed in
580 Choulet et al. (2014). The following evolution may be proposed:

581 (1) During Mesozoic (**Figure 16a**), the opening of the Atlantic Ocean and the Tethys
582 led to the reactivation of Variscan deep structures into normal faults that control the formation
583 of a series of horsts and grabens (Laville and Piqué 1991; Piqué 1994). During the Early
584 Jurassic, the formation of carbonate platforms with reef limestone in shallow domains is
585 accompanied by deposition of Zn-Pb sulphide lenses throughout the future High Atlas domain
586 (Mouguina 2004). These deposits are mainly concordant with the bedding of the host rock
587 (Leblanc 1968). As presented in section 2, discontinuous sedimentation has been recorded
588 afterwards, until Tertiary inversion tectonics (Frizon de la Motte et al. 2009).

589 (2) Between 50 Ma and 35Ma, western Mediterranean domains experienced
590 shortening due to convergence between Europe and Africa (**Figure 16b**). As a consequence,
591 the area has recorded compressive tectonics, leading to the formation of the High Atlas fold-
592 and-thrust belt (Frizon de la Motte et al. 2000; 2009). Reactivation of Liassic normal faults
593 into thrusts has controlled the localisation of narrow anticlines (Teixell et al. 2003), as
594 exemplified at Aït Labbès and Toulal (**Figure 16c**). This compression is not responsible for
595 the present topography but can account for a regional uplift, intense erosion and subsequent
596 exhumation of Zn-Pb sulphide lenses. When the water table has fallen down, dissolution of
597 host limestone may have started, as well as supergene oxidation of the sulphide protore
598 (Choulet et al. 2014). The upright position of the ore lenses has facilitated the downward
599 percolation of the surface water leading to the formation of non-sulphide Zn ore deposits.

600 Coevally, infilling of karst-related cavities has occurred, either as internal karstic
601 sedimentation or as a precipitation from a Zn-rich solution. Both rock types acquired their
602 fabrics, marked by horizontal foliation and lineation tending to be parallel to the trend of
603 dissolution cavities, controlled by the hydrodynamic regime within the karst. Despite a
604 regional arid climate and relatively quiet tectonics between 35Ma and 5Ma (Maley 1980),
605 short wet episodes (Le Houérou 1997) have contributed to enlargement of karst network and
606 deepening of supergene weathering front.

607 (3) Since 3Ma, a second major shortening episode has affected northern Africa
608 (**Figure 16d**; Frizon de Lamotte et al. 2000; 2009). Although this episode is widely observed
609 and responsible for the present topography (**Figure 16e**), it seems that its effects on non-
610 sulphide Zn ore deposits of Moroccan High-Atlas has remained limited, as magnetic foliation
611 and sedimentary bedding are mostly preserved as horizontal. Conversely, at Aït Labbès or at
612 Tadaghast, the absence of a well-defined foliation or the oblique pattern of the fabric may
613 indicate that this second compression episode has modified the AMS and remanent
614 magnetisation primary patterns. The widespread reverse polarities constrain the upper limit
615 for oxidation to 0.78 Ma and the last reversal of the Earth magnetic field.

616

617 **6. Conclusions**

618

619 This is the first attempt of AMS study within non-sulphide Zn ore deposits. It provides
620 crucial information on internal fabrics within ores and on the first-order geometric
621 connections between ore and internal karstic sediment. Results are consistent with field
622 observation and previous interpretations (Choulet et al. 2014). Hence, the dominantly
623 horizontal magnetic foliation and the direction of magnetic lineation that tends to be parallel
624 to the karstic cavities alignment may attest for a control of fabrics by karst hydrodynamics.

625 Locally, rock magnetism signal has been removed or fabrics have been tilted due to late
626 superimposed tectonic events.

627 Palaeomagnetism was successfully applied on both ore and internal karstic sediment
628 from three deposits and obtained results are compatible with age constraints inferred from
629 field observations. Our results support a post-tilting paleomagnetic record that we interpret as
630 of primary origin; it has been acquired either during chemical alteration of ore vein due to
631 rock exhumation or during internal sedimentation processes resulting in the filling of karst-
632 related cavities. Results also suggest local diachronism between deposits, probably due to
633 differences of uplift across the range. However, this last conclusion may be tempered, as our
634 age resolution is not statistically acceptable and we are not able to narrow the time interval
635 between Late Eocene and the last magnetic reversal. The restricted sampling and the limited
636 absolute movement of Africa during the last tens millions years may explain this issue.

637 As inferred by Boni et al. (2005), this study has shown that palaeomagnetism can be
638 used to constrain the timing of supergene oxidation and the formation of non-sulphide ore
639 deposits. In addition, coupling specimens collected from internal karstic sediment and ore
640 may provide robust results, especially when the rock fabric is controlled by AMS parameters
641 and patterns. Although Sardinian and Moroccan deposits are not ideal cases for high
642 resolution dating, this method may be applied on other examples throughout the world
643 (Belgium, Iran, Vietnam…). In the case of historic deposits of Belgium (Dejonghe 1998), this
644 method could be of great benefit, as field observation only provides a timing of formation
645 between Visean and Cretaceous (Coppola et al. 2008). Besides, the occurrence of supergene
646 willemite mineralisation and its possible use for geochronology (Schneider et al. 2008) may
647 represent a good opportunity to compare both methods and assess the utilisation of
648 palaeomagnetism to timely constrain oxidation episodes.

649

7. Acknowledgements

This study has benefited from financial support by the Région Centre and Managem in the frame of the 2011-2013 project "Calamines". Many thanks are due to L. El Hassani, O. Baha and M. Maftou Si Med for field support and for providing access to the different mines. Many thanks are due to B Lehmann and A Cheilletz for handling manuscript and to two anonymous reviewers for their constructive comments that greatly improved the manuscript.

8. References

Agard J, du Dresnay R (1965) La région minéralisée du Jbel Bou-Dahar, près de Beni Tajjit (Haut-Atlas oriental) : Étude géologique et métallogénique. Notes et Mém Serv Géol Maroc 181:135-166 (in French).

Auajjar J, Boulègue J (1999) Les minéralisations Pb-Zn-(Cu) Ba du socle paléozoïque et de la plate-forme liasique du district du Tazekka (Taza, Maroc oriental): une synthèse. Chron Rech Min 536-537:121-135 (in French).

Aubourg C, Pozzi J-P, Kars M (2012) Burial, claystones remagnetization and some consequences for magnetostratigraphy. Geol Soc London, Sp Pub 371:181-188.

Bazin D (1968) Etude géologique et métallogénique des chaînons atlasique du Tizi n'Firest au Nord de Ksar-es-Souk, Maroc. Notes et Mém Serv Géol Maroc 206:37-114 (in French).

673

674 Besse J, Courtillot V (2002) Apparent and true polar wander and the geometry of the
675 geomagnetic field over the last 200 Myr. J Geophys Res 107:doi:10.1029/2000JB000050.

676

677 Boni M, Gilg HA, Aversa G, Balassone G (2003) The "Calamine" of SW Sardinia (Italy):
678 geology, mineralogy and stable isotope geochemistry of a supergene Zn mineralization. Econ
679 Geol 98:731-748.

680

681 Boni M, Dinarès-Turell J, Sagnotti L (2005) Paleomagnetic dating of non-sulfide Zn-Pb ores
682 in SW Sardinia (Italy): a first attempt. Ann of Geoph 48:301-312.

683

684 Boni M, Terracciano R, Evans N, Laukamp C, Schneider J, Bechstädt T (2007) Genesis of
685 vanadium ores in the Otavi Mountainland (Namibia). Econ Geol 102:441-469.

686

687 Boni M, Balassone G, Arseneau V, Schmidt P (2009) The non-sulphide zinc deposit at Accha
688 (Southern Peru): geological and mineralogical characterization. Econ Geol 104:267-289.

689

690 Borg G (2003) Surface-related formation, upgrading, and improvement of ore deposits - a
691 review of supergene metallogenic processes. In: Eliopoulos DG et al. (Ed.), Mineral
692 Exploration and Sustainable Development. Millress, 61-64.

693

694 Borg G, Kärner K, Buxton M, Armstrong R, van der Merve, Schalk W (2003) Geology of the
695 Skorpion non-sulphide deposit, southern Namibia. Econ Geol 98:749-771.

696

697 Borg G (2009) The role of fault structures and deep oxidation in supergene base metal
698 deposits. In: Titley SR (Ed.), Supergene Environments, Processes and Products. Econ Geol
699 Spec Publ 14:121-132.

700

701 Bouchaou L (1988) Hydrogéologie du basin des sources karstiques du complexe calcaire
702 Haut-Atlasien du Dir de Beni-Mellal (Maroc). Dissertation, Université de Besançon (in
703 French).

704

705 Bradley DC, Leach DL (2003) Tectonic controls of Mississippi Valley-type lead-zinc
706 mineralization in orogenic forelands. Miner Deposita 38:652-667.

707

708 Brechbühler YA, Bernasconi R, Schaer JP (1988) Jurassic sediments of the Central High
709 Atlas of Morocco: deposition, burial and erosion history. In: Jacobshagen V (Ed.), The Atlas
710 System of Morocco. Lect Notes Earth Sci 15:139-168.

711

712 Bruyère D, De Putter T, Decrée S, Dupuis C, Fuchs Y, Jamoussi F et al (2010) Miocene
713 karsts and associated Fe-Zn-rich minerals in Aïn Khamouda (Central Tunisia). J Afr Earth Sci
714 57:70-78.

715

716 Caïa J (1968) Roches éruptives basiques et minéralisations en plomb, zinc et strontium de la
717 région de Tirrhist (Haute-Atlas de Midelt). Notes et Mém Serv Géol Maroc 206:7-30 (in
718 French).

719

720 Charles N, Faure M, Chen Y (2009) The mechanism emplacement of the Montagne Noire
721 migmatitic dome (French Massif Central): New insights from petrofabric and AMS studies. J
722 Struct Geol 31:1423-1440.

723

724 Charles N, Gumiaux C, Augier R, Chen Y, Faure M, Lin W, Zhu R (2012) Metamorphic Core
725 Complex dynamics and structural development: Field evidences from the Liaodong Peninsula
726 (East China). Tectonophysics 560-561:22-50.

727

728 Charrière A, Haddoumi H, Mojon PO (2005) Découverte de Jurassique supérieur et d'un
729 niveau marin du Barrémien dans les “couches rouges” continentales du Haut-Atlas central
730 marocain : implications paléogéographiques et structurales. C R Palevol 4:385-394 (in
731 French).

732

733 Charrière A, Haddoumi H, Mojon PO, Ferrière J, Cuche D, Zili L (2009) Mise en évidence
734 par charophytes et ostracodes de l'âge paléocène des dépôts discordants sur les rides
735 anticlinales de la région d'Imilchil (Haut-Atlas, Maroc): conséquences paléogéographiques et
736 structurales. C R Palevol 8:9-19 (in French).

737

738 Chèvremont P (1975) Les roches éruptives basiques des boutonnières de Tassent et Tasraft et
739 leurs indices métallifères dans leur cadre géologique (Haut-Atlas central, Maroc).
740 Dissertation, Université Claude-Bernard, Lyon (in French).

741

742 Choulet F, Charles N, Barbanson L, Branquet Y, Sizaret S, Ennaciri A, Badra L, Chen Y
743 (2014) Non-sulfide zinc deposits of the Moroccan High Atlas: Multi-scale characterization
744 and origin. Ore Geol Rev 56:115-140.

745

746 Cogné JP (2003) PaleoMac: a Macintosh™ application for treating paleomagnetic data and
747 making plate reconstructions. Geochem Geophys Geosyst
748 4(1):1007.doi:10.1029/2001GC000227.

749

750 Cole PM, Sole KC (2002) Solvent extraction in the primary and secondary processing of

751 zinc. J South Afr Inst Min Metall 102:451-456.

752

753 Coppola V, Boni M, Gilg HA, Balassone G, Dejonghe L (2008) The "calamine" nonsulfides
754 Zn-Pb deposits of Belgium: petrographical, mineralogical and geochemical characterization.
755 Ore Geol Rev 33:187-210.

756

757 Couvreur G (1978) Le rôle de la lithologie dans l'évolution des formes karstiques majeures du
758 Haut Atlas central calcaire (Maroc). Rev Geogr Phys 66:309-311 (in French).

759

760 Daliran F, Borg G, Armstrong R, Walther J, Vennemann T, Friese K et al (2009) Non
761 sulphide zinc deposits, Iran - the hypogene emplacement and supergene modification history
762 of the Angouran Zinc Deposit, NW-Iran. Berichte zur Lagerstätten und Rohstoffforschung,
763 57. Bundesanstalt für Geowissenschaften und Rohstoffe, Hannover, 75 p.

764

765 Daliran F, Pride K, Walther J, Berner ZA, Bakker RJ (2013) The Angouran Zn-(Pb) deposit,
766 NW Iran: Evidence for a two stage, hypogene zinc sulphide-zinc carbonate mineralization.
767 Ore Geol Rev 53:373-402.

768

769 Decrée S, Marignac C, De Putter T, Deloule E, Liégeois JP, Demaiffe D (2008) Pb-Zn
770 mineralizations in a Miocene regional extensional context: the case of the Sidi Driss and the
771 Douahria ore deposits (Nefza mining district, N. Tunisia). Ore Geol Rev 34:285-303.

772

773 Decrée S, Ruffet G, De Putter T, Baele JM, Recourt P, Jamoussi et al (2010) Mn oxides as
774 efficient traps for metal pollutants in a polyphase low-temperature Pliocene environment: a
775 case study in the Tamra iron mine, Nefza mining district, Tunisia. J Afr Earth Sci 57:249-261.

776

777 Dejonghe L (1998) Zinc-lead deposits of Belgium. Ore Geol Rev 12:329-354.

778

779 du Dresnay R (1979) Sédiments jurassiques du domaine des chaînes atlasiques du Maroc.
780 Symposium "Sédimentation jurassique ouest-européenne", ASF Publ Spéc 345-365 (in
781 French).

782

783 du Dresnay R (1988) Recent data on the geology of the Middle Atlas (Morocco). In:
784 Jacobshagen V (Ed.), The Atlas System of Morocco. Lect Notes Earth Sci 15:293-320.

785

786 Emberger A (1965) Carte polygénétique des minéralisations plombifères de la Haute
787 Moulouya (gisements d'Aouli, Mibladen et Zaida), Maroc. C R Acad Sci Paris 260:3433-3436
788 (in French).

789

790 Emberger A (1969) Carte des minéralisations plombo-zincifères du Maroc : gîtes et indices
791 renfermant du plomb ou du zinc en élément majeur ou mineur. Notes et Mém Serv Géol
792 Maroc 215 (in French).

793

794 Essalhi M, Sizaret S, Barbanson L, Chen Y, Branquet Y, Panis D, Camps P, Rochette P,
795 Canals A (2009) Track of fluid paleocirculation in dolomite host rock at regional scale by the
796 Anisotropy of Magnetic Susceptibility (AMS): An example from Aptian carbonates of La
797 Florida, Northern Spain. Earth Planet Sci Lett 277:501-513.

798

Essalhi M, Sizaret S, Barbanson L, Chen Y, Lagroix F, Demory F, Nieto JM, Sáez R, Capitán A (2011) A case study of the internal structures of gossans and weathering processes in the Iberian Pyrite Belt using magnetic fabrics and paleomagnetic dating. Mineral Deposita. doi.10.1007/s00126-011-0361-8.

Fisher RA (1953) Dispersion of a sphere. Proc Roy Soc Lond A217, 295-305.

Frizon de Lamotte D, Zizi M, Missenard Y, Hafid M, El Azzouzi M, Charrière A et al (2008) The Atlas system. In: Michard A, Saddiqi O, Chalouan A, Frizon de Lamotte D (Eds.), Continental Evolution: The Geology of Morocco. Structure, Stratigraphy, and Tectonics of the Africa-Atlantic-Mediterranean Triple Junction. Springer-Verlag 133-202.

Frizon de Lamotte D, Leturmy P, Missenard Y, Khomsi S, Ruiz G, Saddiqi O et al (2009) Mesozoic and Cenozoic vertical movements in the Atlas system (Algeria, Morocco, Tunisia): an overview. Tectonophysics 475:9-28.

Gnoinski J (2007) Skorpion zinc: optimization and innovation. J South Afr Instrum Min Metall 107:657-662.

Gomez F, Allmendinger R, Barazangi M, Beauchamp W (2000) Role of the Atlas Mountains (northwest Africa) within the African-Eurasian plate-boundary zone. Geology 28:775-778.

820

821 Gradstein F, Ogg J, Smith A (2004) A geological time scale. Cambridge University Press, 600
822 p.

823

824 Groves I, Carman CE, Dunlap WJ (2003) Geology of the Beltana willemite deposit, Flinders
825 Ranges, South Australia. Econ Geol 98:797-818.

826

827 Haddoumi H, Charrière A, Andreu B, Mojon PO (2008) Les dépôts continentaux du
828 Jurassique moyen au Crétacé inférieur dans le Haut-Atlas oriental (Maroc) :
829 Paléoenvironnements successifs et signification paléogéographique. Carnets de Géologie -
830 Notebooks on Geology, Brest. (2008/XX (CG2008 AXX).
831 http://paleopolis.rediris.es/cg/French).

832

833 Herbig HG, Trappe J (1994) Stratigraphy of the Subatlas Group (Maastrichtian-Middle
834 Eocene, Morocco). Newsl Stratigr 30:125-165.

835

836 Heyl AV, Bozion CN (1962) Oxidized zinc deposits of the United States, part 1. General
837 geology. US Geol Surv Bull 1135-A, 52 p.

838

839 Hitzman MW, Reynolds NA, Sangster DF, Allen CR, Carman CE (2003) Classification,
840 genesis, and exploration guides for non sulfide zinc deposits. Econ Geol 98:685-714.

841

842 Hosseini SH (2008) Physicochemical Studies of Oxide Zinc Mineral Flotation. Dissertation,
843 University of Technology, Luleå.

844

845 Hrouda F (1982) Magnetic anisotropy of rocks and its application in geology and geophysics.
846 Geophys Surv 5:37-82.

847

848 Jelinek V (1981) Characterization of the magnetic fabric of rocks. Tectonophysics 79:63-67.

849

850 Jemmali N, Souissi F, Vennemann TWM, Carranza EJ (2011) Genesis of the Jurassic
851 carbonate-hosted Pb-Zn deposits of Jebel Ressas (North-Eastern Tunisia): Evidence from
852 mineralogy, petrography and trace metal contents and isotope (O, C, S, Pb) geochemistry. Res
853 Geol 61:367-383.

854

855 Kirschvink J (1980) The least squares line and the analysis of palaeomagnetic data. Geophys J
856 R Astron Soc 62:699-718.

857

858 Large D (2001) The geology of non-sulphide zinc deposits - an overview. Erzmetall 54:264-
859 276.

860

Laville E, Piqué A (1991) La distension crustale atlantique et atlasique au Maroc au début du Mésozoïque: le rejeu des structures hercyniennes. Bull Soc Géol Fr 162:1161-1171.

Laville E, Piqué A (1992) Jurassic penetrative deformation and Cenozoic uplift in the central High Atlas (Morocco): a tectonic model. Structural and orogenic inversions. Geol Rundsch 81:157-170.

Laville E, Piqué A, Amrhar M, Charroud M (2004) A restatement of the Mesozoic Atlasic rifting (Morocco). J Afr Earth Sci 38:145-153.

Leach DL, Bradley D, Lewchuk MT, Symons DTA., de Marsily G, Brannon J (2001) Mississipi Valley-type lead-zinc deposits through geological time: Implications from recent age dating research. Mineral Deposita 36:711-740.

Leblanc M (1968) Etude géologique et métallogénique du Jbel Bou Arhous et de son prolongement oriental (Haut-Atlas marocain oriental). Notes Mém Serv Géol Maroc 206:117-206 (in French).

Le Houérou HN (1997) Climate, flora and fauna changes in the Sahara over the past 500 million years. J Arid Env 37:619-647.

882 Maley J (1980) Les changements climatiques de la fin du Tertiaire en Afrique: leurs
883 conséquences sur l'apparition du Sahara et de sa végétation. In: Williams AJ, Faure H (Eds),
884 The Sahara and the Nile. Balkema, Rotterdam, 63-86.

885

886 Mattauer M, Tapponnier P, Proust F (1977) Sur les mécanismes de formation des chaînes
887 intracontinentales. L'exemple des chaînes atlasiques du Maroc. Bull Soc Géol Fr 19:521-526.

888

889 McFadden PL McElhinny MW (1990) Classification of the reversal test in palaeomagnetism.
890 Geophys J Int 103: 725-729.

891

892 Mouguina EM (2004) Les minéralisations polymétalliques (Zn-Pb, Cu, Co, Ni) du Jurassique
893 du Haut Atlas central (Maroc): Contexte géodynamique, typologies et modèles génétiques.
894 Dissertation, Faculté des Sciences Semlalia, Marrakech.

895

896 Nicod J (1997) Karsts et fonctionnement hydrologique dans le Haut Atlas central calcaire et
897 sur la bordure du Moyen Atlas méridional. Ann Geogr 106 :536-538 (in French).

898

899 Ovtracht A (1978) Province plombo-zincifère du Haut Atlas central. Mines Géol Energie
900 44:103-109.

901

902 Pannalal SJ, Symons DTA, Sangster DF (2008) Paleomagnetic Evidence for an Early Permian
903 Age of the Lisheen Zn-Pb Deposit, Ireland. Econ Geol 103:1641-1655.

904

905 Piqué A, Michard A (1989) Moroccan Hercynides: a synopsis. The Paleozoic sedimentary
906 and tectonic evolution at the northern margin of West Africa. Am J Sci 289:286-330.

907

908 Piqué A (1994) Géologie du Maroc, les domaines régionaux et leur évolution structurale.
909 Pumag, Marrakech.

910

911 Popov A (1968) Les types morphologiques et la répartition des gisements de zinc et de plomb
912 en Algérie. Ann Min Géol 23:103-203.

913

914 Reichert J, Borg G (2008) Numerical simulation and a geochemical model of supergene
915 carbonate-hosted non-sulphide zinc deposits. Ore Geol Rev 33:134-151.

916

917 Ricordel C (2007) Datations par paléomagnétisme des paléoaltérations du Massif central et de
918 ses bordures: Implications géodynamiques. Dissertation, Ecole des Mines de Paris.

919

920 Ricordel-Prognon C, Lagroix F, Moreau MG, Thiry M (2010) Lateritic paleoweathering
921 profiles in French Massif Central: Paleomagnetic datings. J Geophys Res 115,
922 doi:10.1029/2010JB007419.

923

924 Rochette P, Jackson M, Aubourg C (1992) Rock magnetism and the interpretation of the
925 anisotropy of magnetic susceptibility. Rev Geophys 30:209-226.

926

927 Rouvier H, Perthuisot V, Mansouri A (1985) Pb-Zn deposits and salt-bearing diapirs in
928 Southern Europe and North Africa. Econ Geol 80:666-687.

929

930 Santoro L, Boni M, Herrington R, Clegg A (2013) The Hakkari nonsulfide Zn–Pb deposit in
931 the context of other non sulfide Zn-Pb deposits in the Tethyan Metallogenetic Belt of Turkey.
932 Ore Geol Rev. doi.org/10.1016/j.oregeorev.2013.01.011.

933

934 Schneider J, Boni M, Laukamp C, Bechstädt T, Petzel V (2008) Willemite (Zn_2SiO_4) as a
935 possible Rb-Sr geochronometer for dating nonsulfide Zn-Pb mineralization: Examples from
936 the Otavi Mountainland (Namibia). Ore Geol Rev 33:152-167.

937

938 Sizaret S, Chen Y, Chauvet A, Marcoux E, Touray JC (2003) Magnetic fabrics and fluid flow
939 directions in hydrothermal systems. A case study in the Chaillac Ba-F-Fe deposit (France).
940 Earth Plan Sci Lett 206:555-570.

941

942 Symons DTA, Sangster DF, Leach DL (1996) Paleomagnetic dating of Mississippi Valley-
943 type Pb-Zn-Ba deposits. Soc Econ Geol Spec Vol 4:515-526.

944

945 Symons DTA, Stratakos KK (2000) Palaeomagnetic dating of dolomitization and Mississippi
946 Valley-type zinc mineralization in the Mascot-Jefferson city district of Eastern Tennessee: a
947 preliminary analysis. In: Pueyo JJ, Cardellach E, Bitzer K, Taberner C (Ed), Geofluids III, 3rd
948 International Conference on Fluid Evolution, Migration and Interaction in Sedimentary
949 Basins and Orogenic Belts. J Geochem Explor 69-70:373-376.

950

951 Symons DTA, Smethurst MT, Ashton JH (2002). Paleomagnetism of the Navan Zn-Pb
952 Deposit, Ireland. Econ Geol 97:997-1012.

953

954 Tarling DH, Hrouda F (1993) The magnetic anisotropy of rocks. Chapman and Hall, London.

955

956 Terracciano R (2008) Willemite mineralization in Namibia and Zambia. Dissertation,
957 University of Napoli.

958

959 Théveniaut H, Freyssinet P (1999) Paleomagnetism applied to lateritic profiles to assess
960 saprolite and duricrust formation processes: The example of the Mont Baduel profile (French
961 Guiana). Palaeogeogr Palaeoclimatol Palaeoecol 148:209-231.

962

963 Théveniaut H, Freyssinet P (2002) Timing of lateritization on the Guiana Shield: Synthesis of
964 paleomagnetic results from French Guiana and Suriname. Palaeogeogr Palaeoclimatol
965 Palaeoecol 178:91-117.

966

967 Théveniaut H, Quesnel F, Wyns R, Hugues G (2007) Paleomagnetism dating of the "Borne de
968 Fer" ferricrete (NE France): Lower Cretaceous continental weathering. Palaeogeogr
969 Palaeoclimatol Palaeoecol 253:271-279.

970

971 Van der Voo R (1993) Paleomagnetism of the Atlantic, Tethys and Iapetus Oceans.
972 Cambridge University Press, New York, 411 p.

973

974 Withney DL, Evans B (2010) Abbreviations for names of rock-forming minerals. Am Miner
975 95:185-187.

976

977 Zijderveld JDA (1967) A.C. demagnetization of rocks: Analysis of results. Methods in
978 Paleomagnetism Conference, Amsterdam, Proceedings 254-286.

Figure captions

Figure 1: (a) Simplified tectonic map of western Mediterranean Sea and western North Africa, illustrating the relationships between High Atlas and the Alpine Belt (modified from Gomez et al. 2000). MA: Middle Atlas. (b) Geological map of the Moroccan High Atlas. The location of the Pb-Zn prospects (white circle) and studied ore deposits (yellow star) is also indicated. (c) Cross-section of the Moroccan High Atlas, illustrating the structure of the fold-and-thrust belt and the connection between the Mesozoic cover and the Palaeozoic basement (modified after Teixell et al. 2003).

Figure 2: (a) Panoramic view showing the typical fold-and-thrust structure of the Moroccan High-Atlas with tight and faulted anticline (Aït Labbès ore deposit). (b) View of a karstic cavity, parallel to the N80°E anticline structure, and filled by red calamine during ore extraction (Aït Labbès ore deposit). (c) Aspect of the calamine network, forming N70°E-striking boudin-like veins (Toulal prospect). (d) View of the cavities, previously filled by red ore (Toulal prospect). (e) View of a profile showing stratabound mineralisation, with distribution of Zn-Pb sulphides minerals (bottom) and Zn-Pb non-sulphides minerals (top) (Tadaghast ore deposit). (f) Relation between tilted limestone strata and horizontal marl of internal sediments filling a karstic cavity whose limit is indicated by red dashed line (Toulal prospect). (g) Sample of Zn sulphides and non-sulphides minerals (sphalerite ZnS, smithsonite $ZnCO_3$, Fe-oxides, and hemimorphite $Zn_4Si_2O_7(OH)_2 \cdot (H_2O)$) from Toulal. (h) Red ore sample made of smithsonite and Fe-oxides from Aït Labbès ore deposit. (i) Grey ore sample made of smithsonite, hemimorphite and hydrozincite ($Zn_5(CO_3)_2(OH)_6$) from Beni Tajite ore deposit. Abbreviations for minerals according to Whitney and Evans (2010): Gn: galena, Hmp: hemimorphite, Hyd: hydrozincite, Sp: sphalerite.

Figure 3: Microphotographs of non-sulphide Zn-Pb ores (a to d) and karst internal sediments (e and f) from studied ore deposits. (a) Relics of sphalerite and pyrite (protore) associated with translucent smithsonite. (TL, nic. //). (b) Iron oxi-hydroxides (goethite and hematite) encrusting oxidized smithsonite, both constituting the "red calamine" (RL, nic. //). (c) Alteration stage II smithsonite ("grey ore") growing on primary oxidized stage I smithsonite and postdating the formation of iron oxi-hydroxides. The final filling is made of hemimorphite and calcite (RL, nic. +). (d) "Grey ore" with alteration stage II smithsonite encrusting alteration stage I smithsonite and iron oxides (TL, nic. //). Zoom box: concentric shells of goethite rhythmically encrusting translucent smithsonite (TL, nic. +). (e) Internal sediments: banded Fe-oxides (hematite and goethite) encrusting banded calcite. Others micro-beds are made of smithsonite and Fe-oxides clasts. Note the presence of a smithsonite clast. (TL, nic. +). (f) Zoom on a clastic micro-bed within internal sediments. Clasts of Fe-oxides are cemented by calcite (TL, nic. //). (g) Synoptic paragenetic sequence of observed minerals in studied ore deposits. Vertical lines represent the separation between the protore mineralisation (sulphides) and the two supergene stages (i.e. red-ore and grey-ore). Vertical dashed line corresponds to the limit between the "red ore" and the "grey ore" (modified after Choulet et al. 2014). Mineral abbreviations according to Whitney and Evans (2010): Cal: calcite, Gth: goethite, Hem: hematite, Hmp: hemimorphite, Py: pyrite, Qz: quartz, Sm: smithsonite, Sp: sphalerite. RL: reflected light, TL: transmitted light, nic. //: plane polarized light, nic. +: crossed polarized light.

Figure 4: AMS and palaeomagnetic sampling sites. (a to d) Aït Labbès ore deposit sampling sites. In the sampled zone, the dip of the limestone is about 20° to the NW. (e and f) Toulal prospect sampling sites. (g) Beni Tajite ore deposit with localisation of sampling sites within

1029 galleries. (h and i) Tadaghast ore deposit sampling sites into mineralised E-W vein (h) and
1030 horizon (i).
1031
1032 **Figure 5**: X-ray diffraction patterns of rock powders from Aït Labbès (a), Toulal (b), Beni
1033 Tajite (c) and Tadaghast (d) ore deposits. Intensities (y axis) are normalised to the value of the
1034 highest peak.
1035
1036 **Figure 6**: Histogram of bulk magnetic susceptibility (K_m) of all measured samples.
1037
1038 **Figure 7**: Results of Isothermal Remanent Magnetization (IRM) measurements.
1039
1040 **Figure 8**: Results of magnetic remanence measurements (a to c and e to g) and
1041 thermomagnetic Curie temperature analyses (d and h) for samples of red calamine and
1042 internal sediments from Aït Labbès, Toulal and Tadaghast. Abbreviations: HC: heating
1043 component, CC: cooling component.
1044
1045 **Figure 9**: AMS results from Aït Labbès deposit (a) and Toulal prospect (b) for non-sulphide
1046 Zn ore, internal sediments and host-rock. Results are represented by equal-area projection of
1047 each site. Squares, triangles and circles stand for K_1 (magnetic lineation), K_2 (intermediate
1048 axis) and K_3 (pole of magnetic foliation), respectively. Small grey dots and larger black ones
1049 represent individual specimen and site-mean direction, respectively. Confidence ellipses at
1050 95% level are drawn for each site-mean direction. AMS scalar parameters are represented by
1051 graphs: T (shape parameter) *vs.* P_J (corrected anisotropy parameter), T *vs.* K_m (mean bulk
1052 magnetic susceptibility) and P_J *vs.* K_m. Calculations of T and P_J can be found in Jelinek

(1981). Red line indicates the karst cavity azimuth (~N50° for Aït Labbès and ~N80° for Toulal).

Figure 10: AMS results for Beni Tajite deposit (a) and Tadaghast deposit (b). See Figure 9 for details.

Figure 11: Palaeomagnetic results for the Aït Labbès deposit. Orthogonal projections of sample demagnetization (Zijderveld 1967) show reverse (a) or normal (b) polarity for red ore (a) and reverse or normal (d) polarity for internal sediments. Equal-area projections show red ore (c) and internal sediments (e) specimen directions (grey dots) with locality-mean direction (black star), isolated from high temperature or high coercive AF components. Black diamond indicates the position of present-day earth magnetic field.

Figure 12: Palaeomagnetic results for the Toulal prospect. Orthogonal projections of sample demagnetization (Zijderveld 1967) show normal (a) or reverse (b) polarity for red ore and normal (d) and reverse (e) polarity for internal sediments. Equal-area projections show red ore (c) and internal sediments (f) specimen directions (grey dots) with locality-mean direction (black star), isolated from high temperature or high coercive AF components. Black diamond indicates the position of present-day earth magnetic field.

Figure 13: Palaeomagnetic results for the Tadaghast deposit (a to d) and Beni Tajite (e and f). Orthogonal projections of sample demagnetization (Zijderveld 1967) showing reverse polarity for red ore (a) and normal polarity for internal sediments (c). Equal-area projections show red ore (b) and internal sediments (d) specimen directions (grey dots) with locality-mean direction (black star), isolated from high temperature or high coercive AF components. Orthogonal

projections of sample demagnetization for Beni Tajite grey ore (e). Equal-area projections of Beni Tajite grey ore shows scattering of data (f). Black diamond indicates the position of present-day earth magnetic field.

Figure 14: Equal-area projection of specimen remanence directions for both red ore (circles) and internal sediment (triangles) for Aït Labbès (a) and Toulal (b). Stars represent the locality-mean direction.

Figure 15: Palaeomagnetic poles calculated for Aït Labbès and Toulal compared to the APWP of Africa between 100 and 10 Ma (Besse and Courtillot 2002). It appears Aït Labbès and Toulal ore deposits are diachronic.

Figure 16: Tectonic sketches illustrating the development of the non-sulphide Zn-Pb deposits during the evolution of the Moroccan High Atlas with the western Mediterranean area (modified from Choulet et al. 2014, Jolivet et al. 2000; Frizon de Lamotte et al. 2000; 2009). (a) The opening of Atlantic Ocean and Tethys is accommodated by normal faulting. This period corresponds to deposition of reef and para-reef limestones and formation of sulphide lenses. (b and c) During Eocene, normal faults were reactivated as thrusts that accommodate the formation of tight anticlines, related to the High-Atlas intra-continental belt. (d and e) Atlasic main folding stage has involved a verticalization of the stratabound lenses of sulphides and has been followed by successive uplift periods, until Present, which have facilitated the percolation of meteoritic water, the karst formation (deposition of internal sediment) and the coeval to subsequent replacement of sulphide ores by non-sulphides ores.

Table 1: AMS results from red and white ores, internal sediments and host limestone. n: number of specimen taken into statistic calculation; N: number of measured specimen. D, I, α_{95min}, α_{95max} are declination, inclination, Jelinek's statistic confidence at 95% level (Jelinek 1981) in degrees, respectively. P_J: Corrected anisotropy degree, T: Anisotropy shape parameter (Jelinek 1981), and K_m: Mean magnetic susceptibility.

Table 2: Palaeomagnetic results from red ore and internal sediments samples collected in the Moroccan High Atlas. n is the number of steps used in Kirschvink's principal component analysis (PCA), N is the number of specimens used for calculation specimen-mean direction, D and I are the respective declination and inclination of the remanent magnetization, MAD is the main angle deviation obtained from PCA, k is the precision parameter and α_{95} is the radius of the 95% confidence circle.

Figure 1

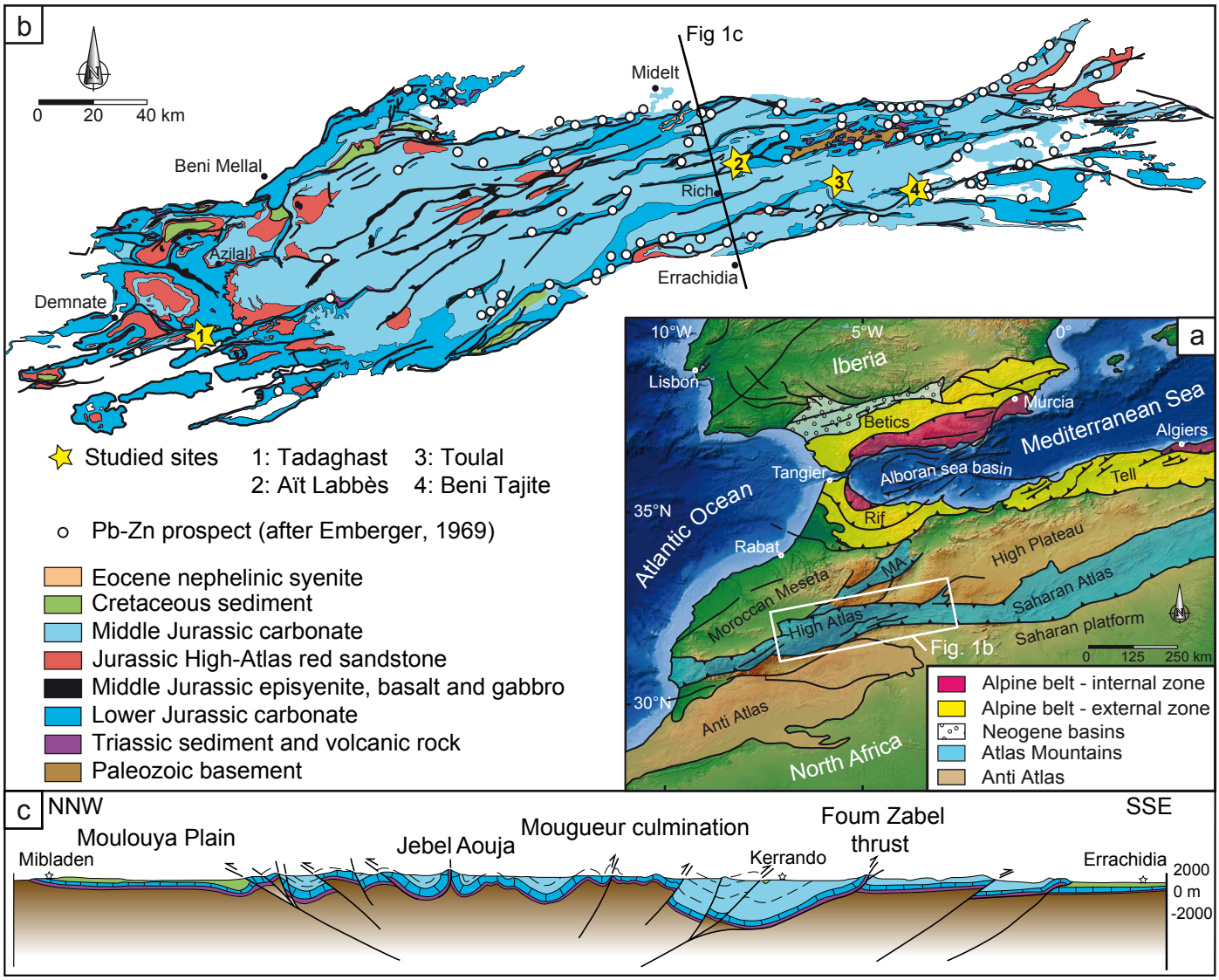

Figure 1

Figure 2

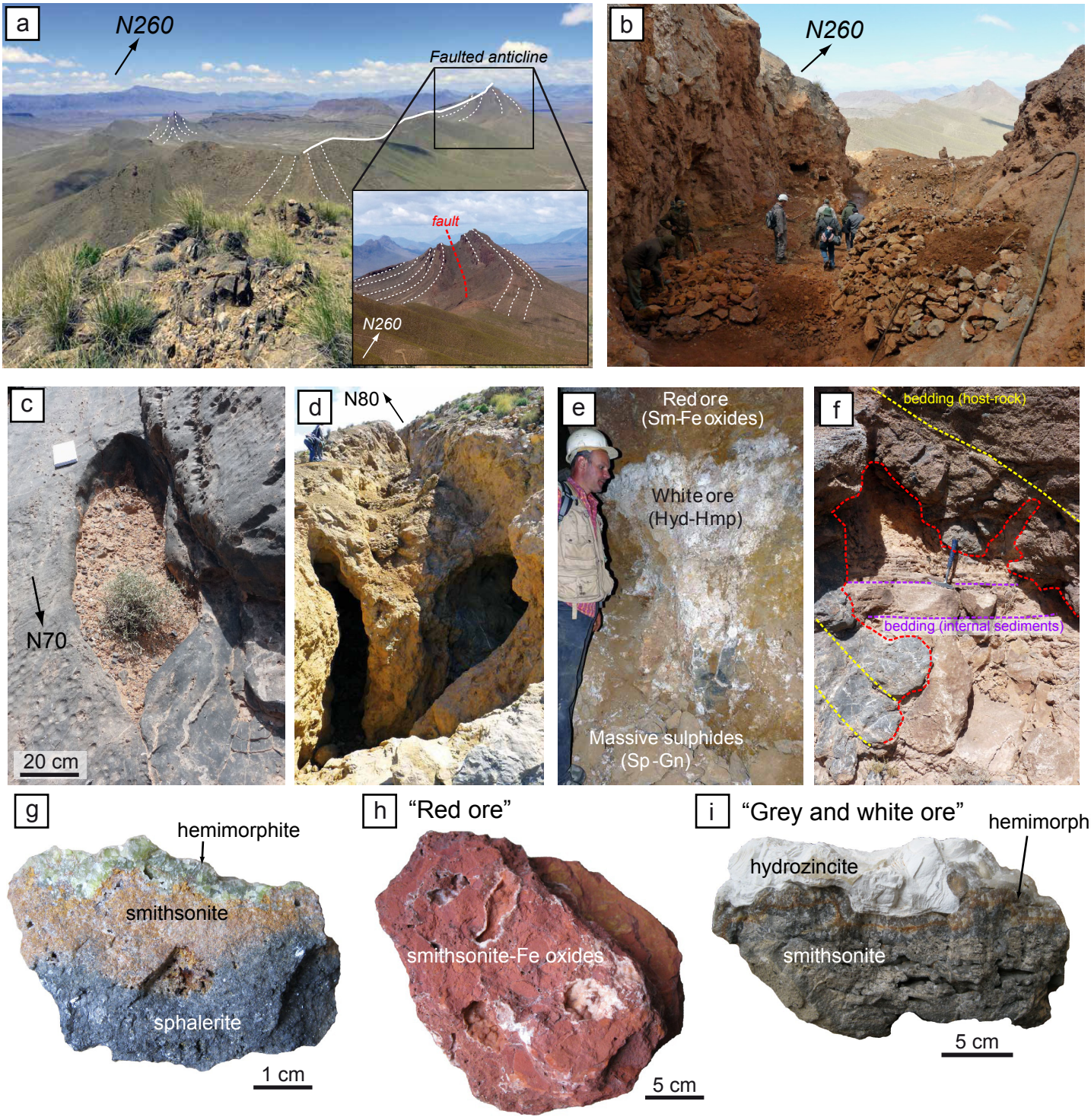

Figure 2

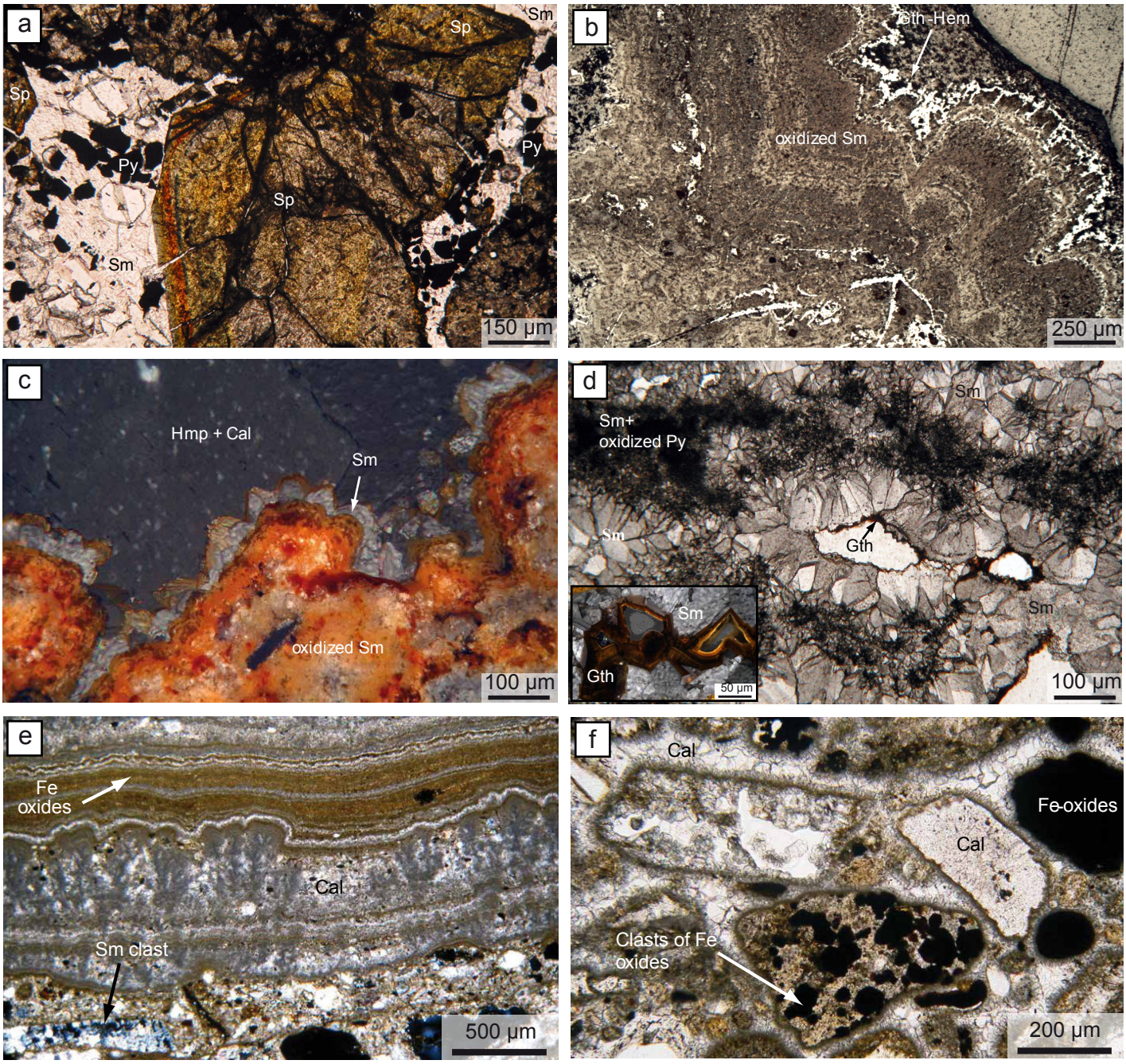
a
Sm
Sp
Sp
Py
Py
Sp
Sm
150 µm
b
Gth-Hem
oxidized Sm
250 µm
c
Hmp + Cal
Sm
oxidized Sm
100 µm
d
Sm
Sm+
oxidized Py
Sm
Gth
Sm
Sm
Gth
50 µm
100 µm
e
Fe
oxides
Cal
Sm clast
500 µm
f
Cal
Fe-oxides
Cal
Clasts of Fe
oxides
200 µm

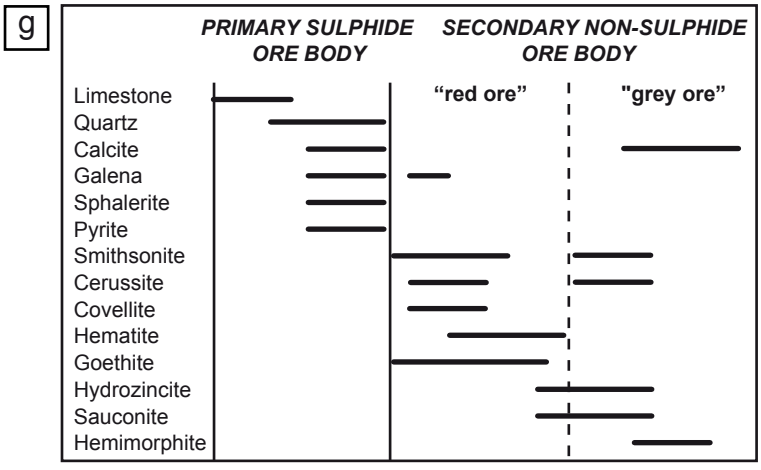
g
PRIMARY SULPHIDE ORE BODY
SECONDARY NON-SULPHIDE ORE BODY
"red ore"
"grey ore"
Limestone
Quartz
Calcite
Galena
Sphalerite
Pyrite
Smithsonite
Cerussite
Covellite
Hematite
Goethite
Hydrozincite
Sauconite
Hemimorphite

Figure 3

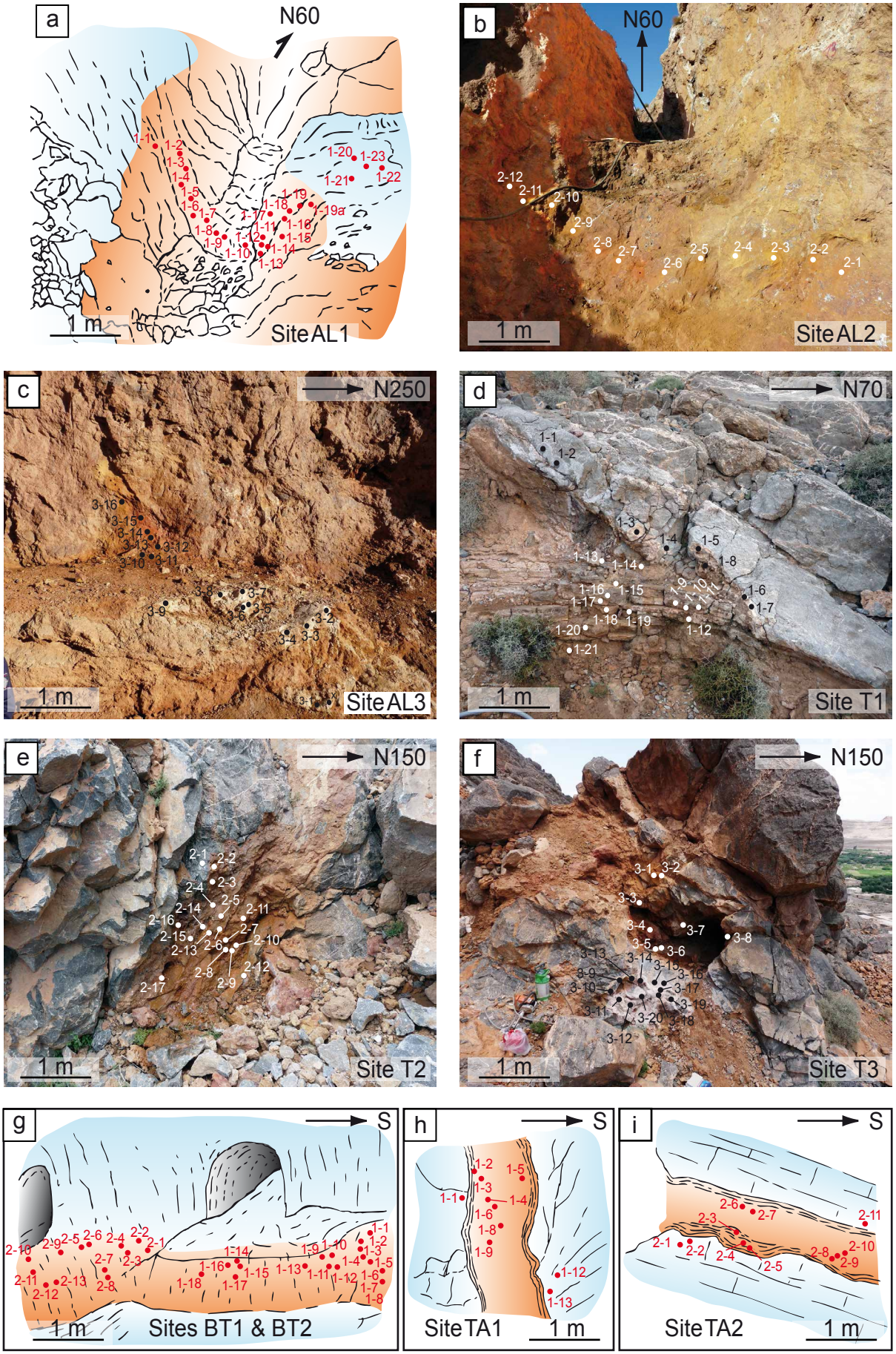
a
N60
1 m
Site AL1
b
N60
1 m
Site AL2
c
N250
1 m
Site AL3
d
N70
1 m
Site T1
e
N150
1 m
Site T2
f
N150
1 m
Site T3
g
S
1 m
Sites BT1 & BT2
h
S
Site TA1
1 m
i
S
Site TA2
1 m

Figure 4

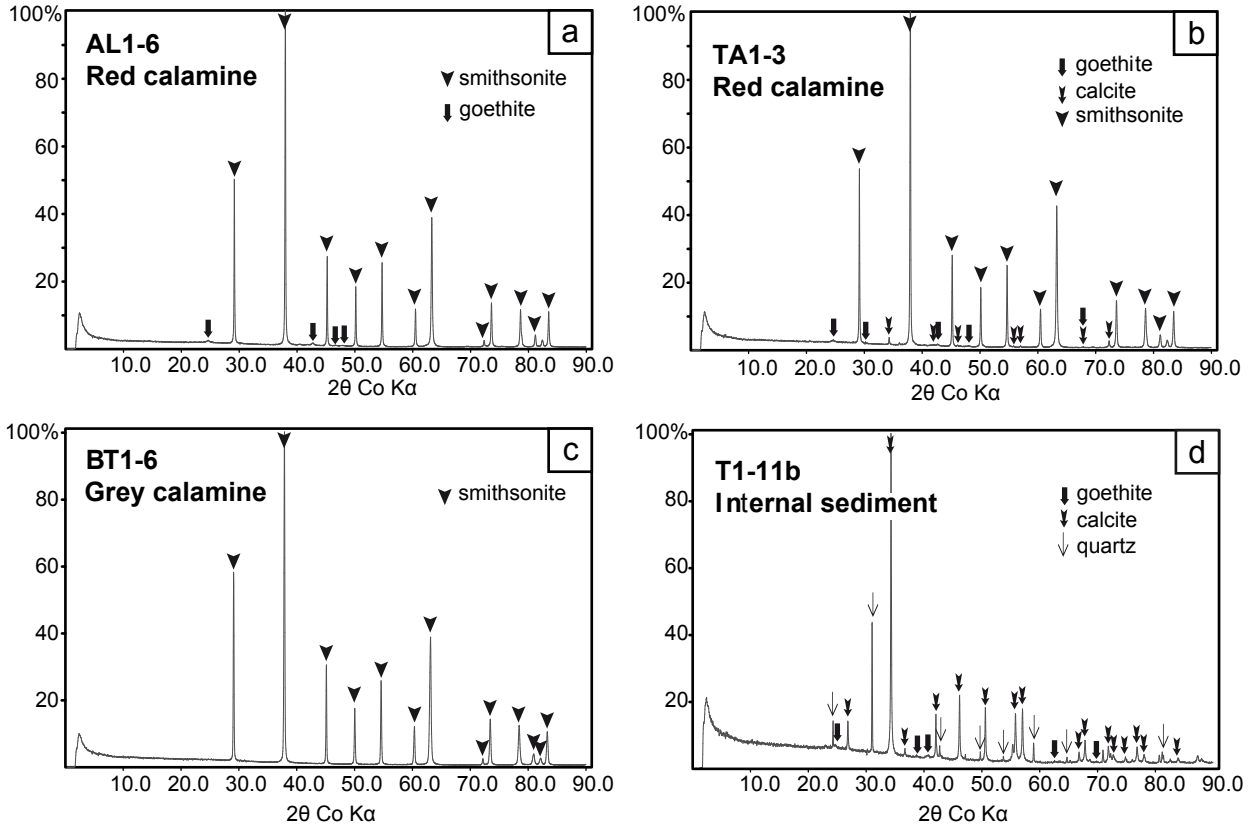
100%
80
60
40
20
AL1-6
Red calamine
a
smithsonite
goethite
10.0 20.0 30.0 40.0 50.0 60.0 70.0 80.0 90.0
2θ Co Kα
TA1-3
Red calamine
b
goethite
calcite
smithsonite
BT1-6
Grey calamine
c
T1-11b
Internal sediment
d
quartz

Figure 5

Figure 6

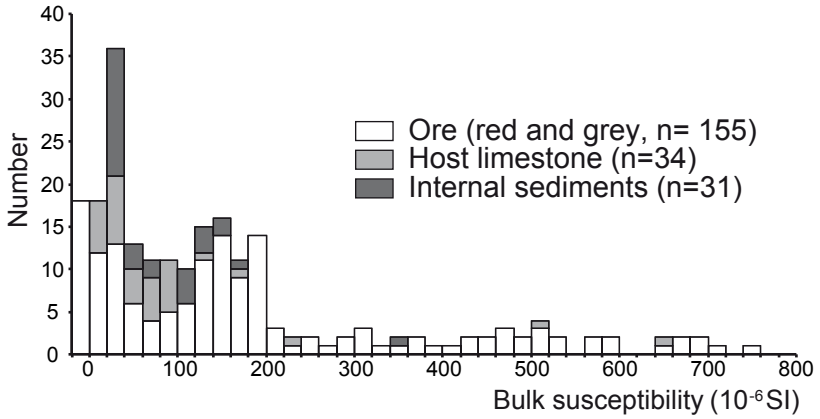

Figure 6

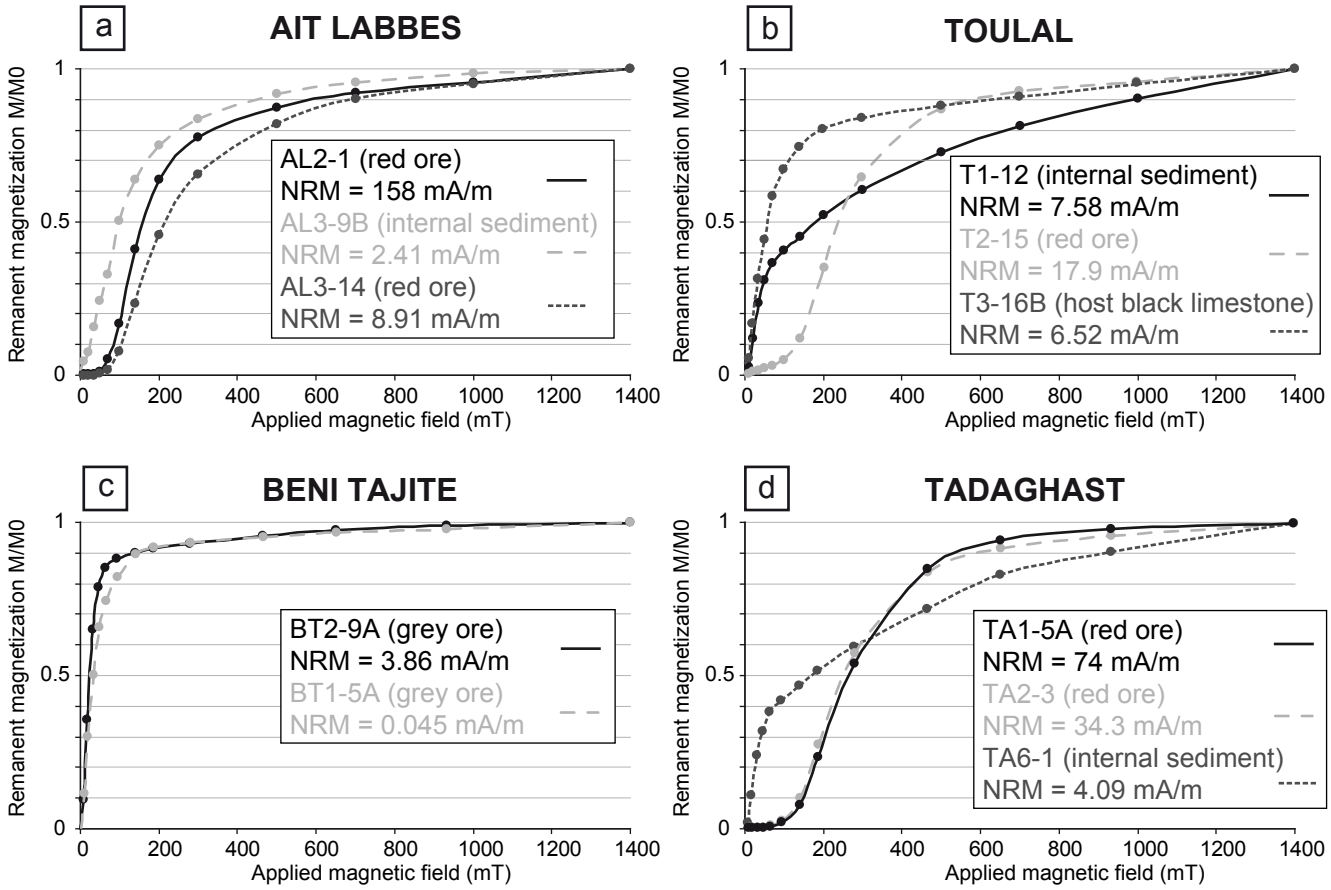
a
AIT LABBES
Remanent magnetization M/M0
Applied magnetic field (mT)
AL2-1 (red ore)
NRM = 158 mA/m
AL3-9B (internal sediment)
NRM = 2.41 mA/m
AL3-14 (red ore)
NRM = 8.91 mA/m
b
TOULAL
T1-12 (internal sediment)
NRM = 7.58 mA/m
T2-15 (red ore)
NRM = 17.9 mA/m
T3-16B (host black limestone)
NRM = 6.52 mA/m
c
BENI TAJITE
BT2-9A (grey ore)
NRM = 3.86 mA/m
BT1-5A (grey ore)
NRM = 0.045 mA/m
d
TADAGHAST
TA1-5A (red ore)
NRM = 74 mA/m
TA2-3 (red ore)
NRM = 34.3 mA/m
TA6-1 (internal sediment)
NRM = 4.09 mA/m

Figure 7

Figure 8

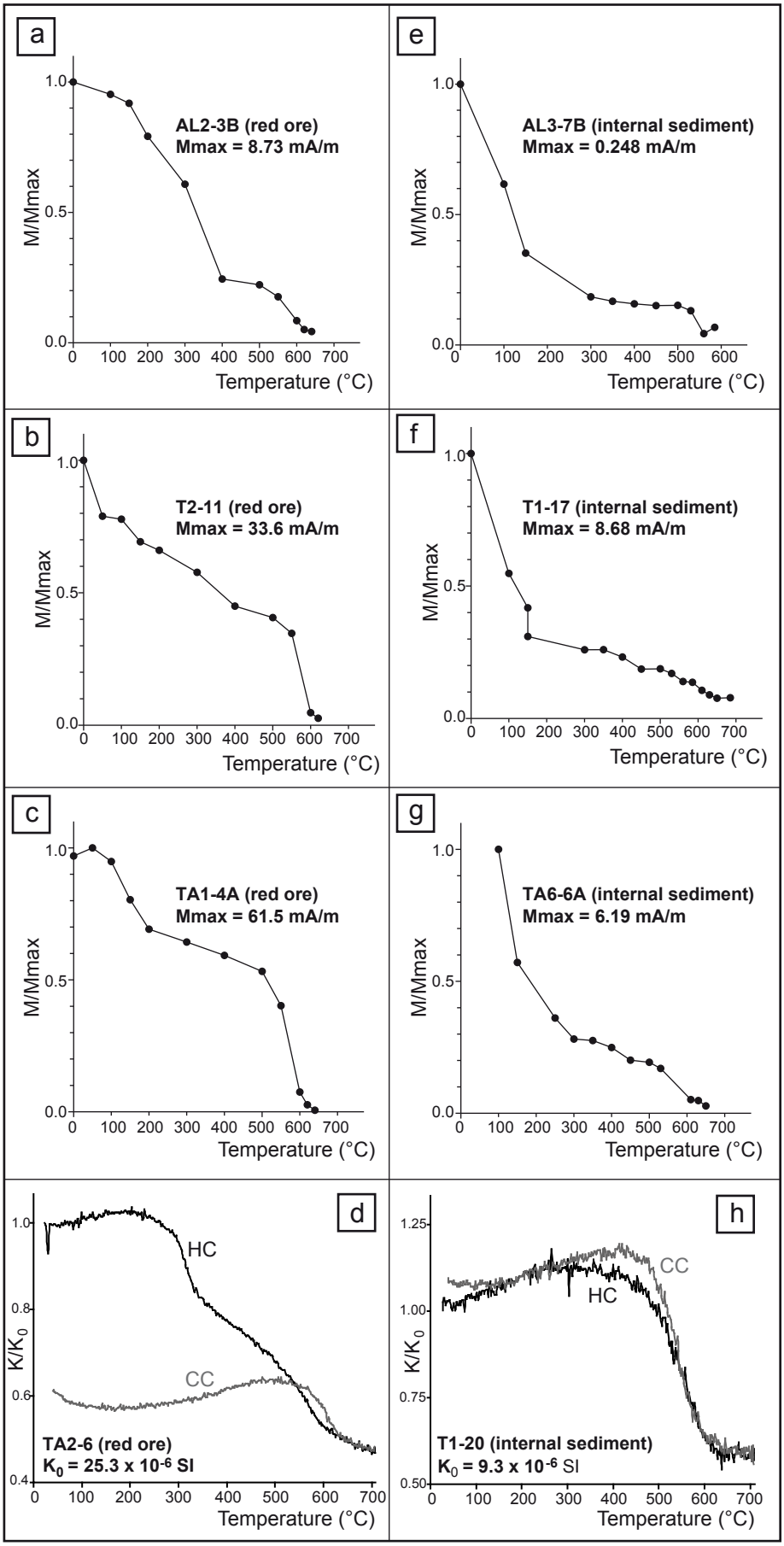

Figure 8

Figure 9

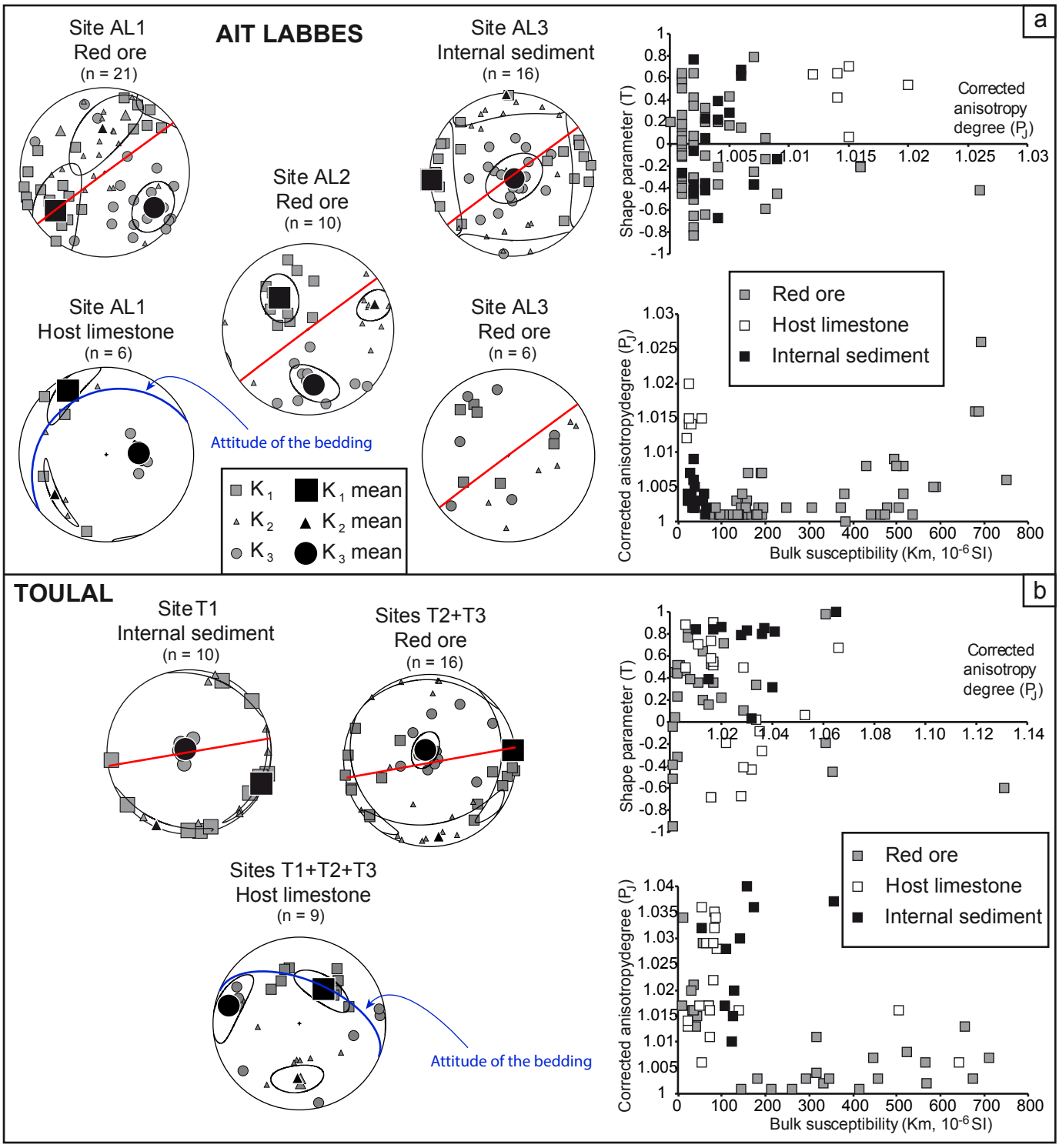

Figure 9

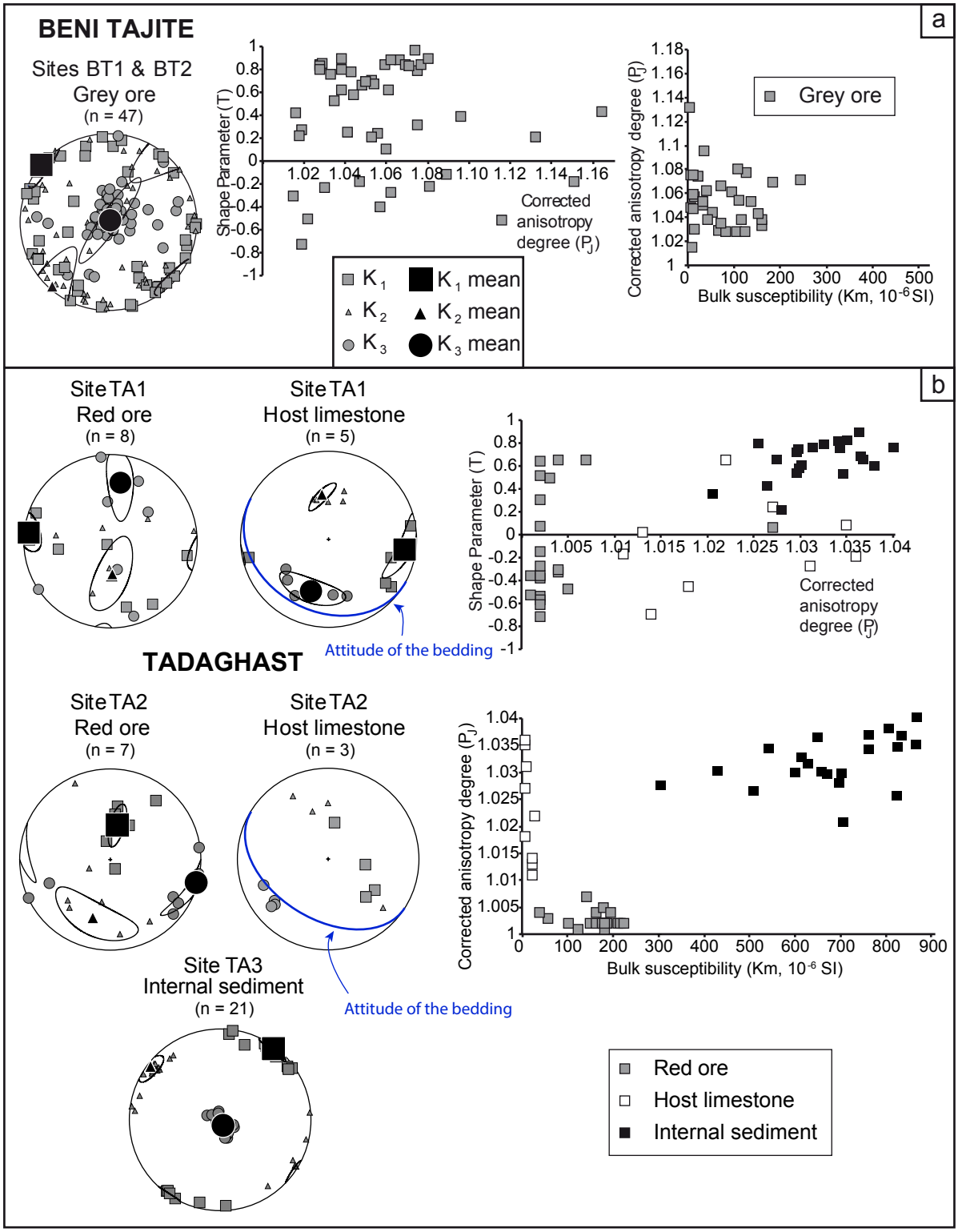
a
BENI TAJITE
Sites BT1 & BT2
Grey ore
(n = 47)
Shape Parameter (T)
Corrected anisotropy degree (Pj)
K1
K2
K3
K1 mean
K2 mean
K3 mean
Corrected anisotropy degree (Pj)
Grey ore
Bulk susceptibility (Km, 10-6 SI)
b
Site TA1
Red ore
(n = 8)
Site TA1
Host limestone
(n = 5)
Attitude of the bedding
Shape Parameter (T)
Corrected anisotropy degree (Pj)
TADAGHAST
Site TA2
Red ore
(n = 7)
Site TA2
Host limestone
(n = 3)
Site TA3
Internal sediment
(n = 21)
Attitude of the bedding
Corrected anisotropy degree (Pj)
Bulk susceptibility (Km, 10-6 SI)
Red ore
Host limestone
Internal sediment

Figure 10

Figure 11

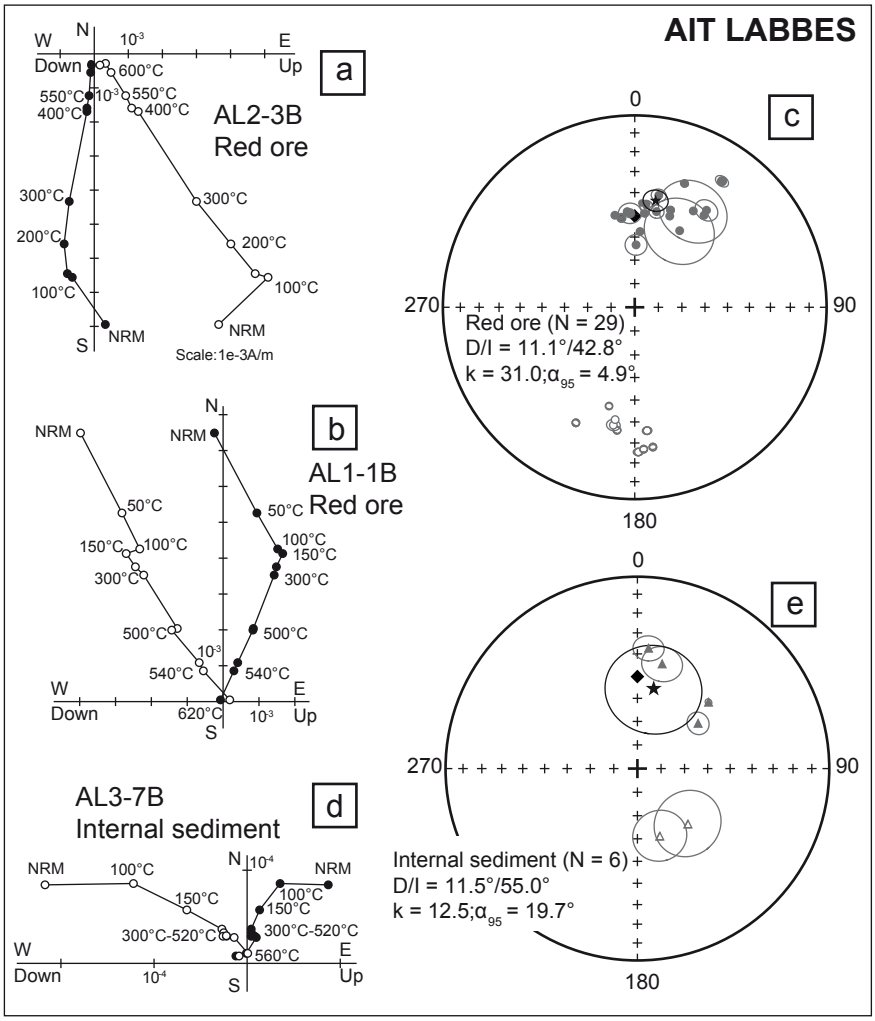

Figure11

Figure 12

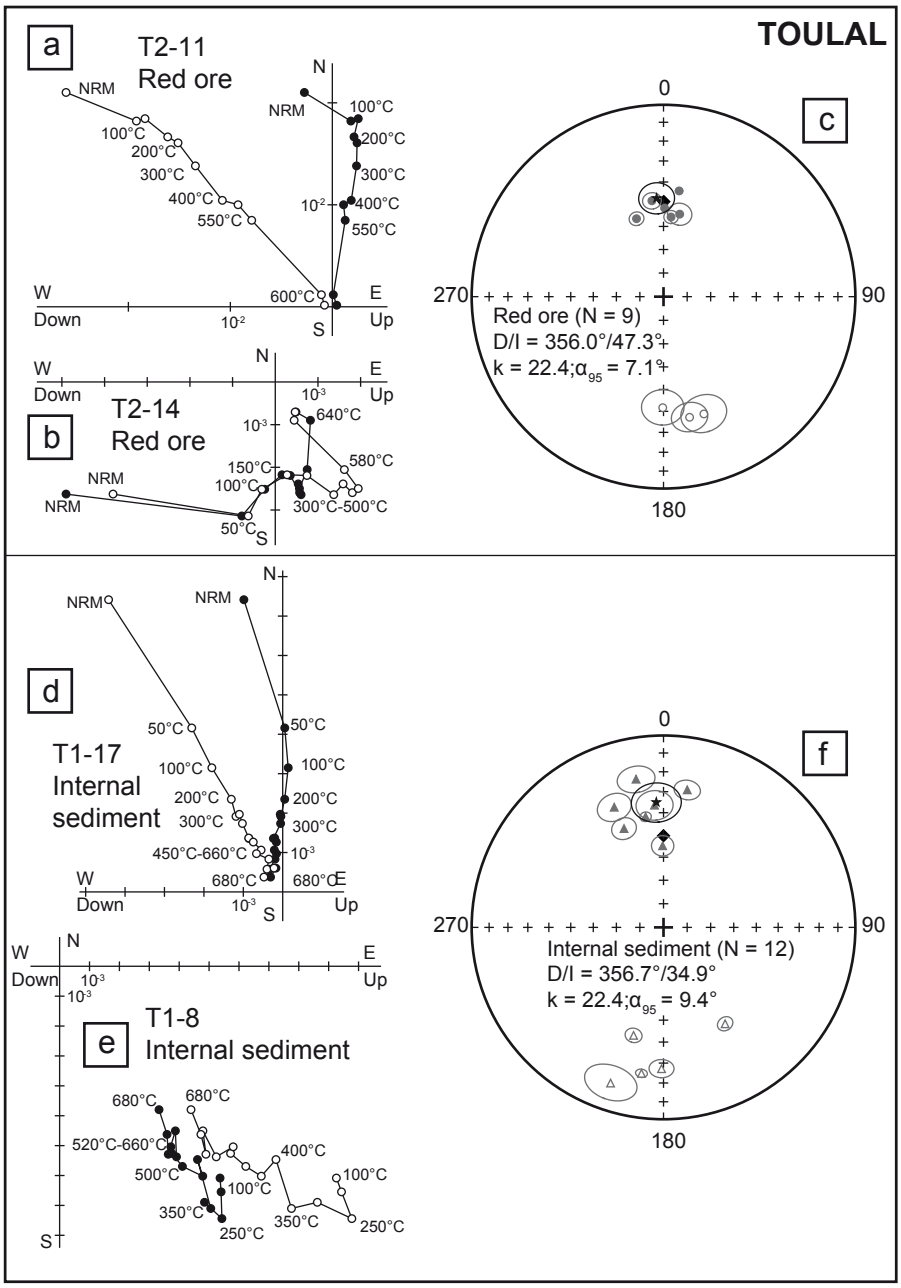

Figure 12

Figure 13

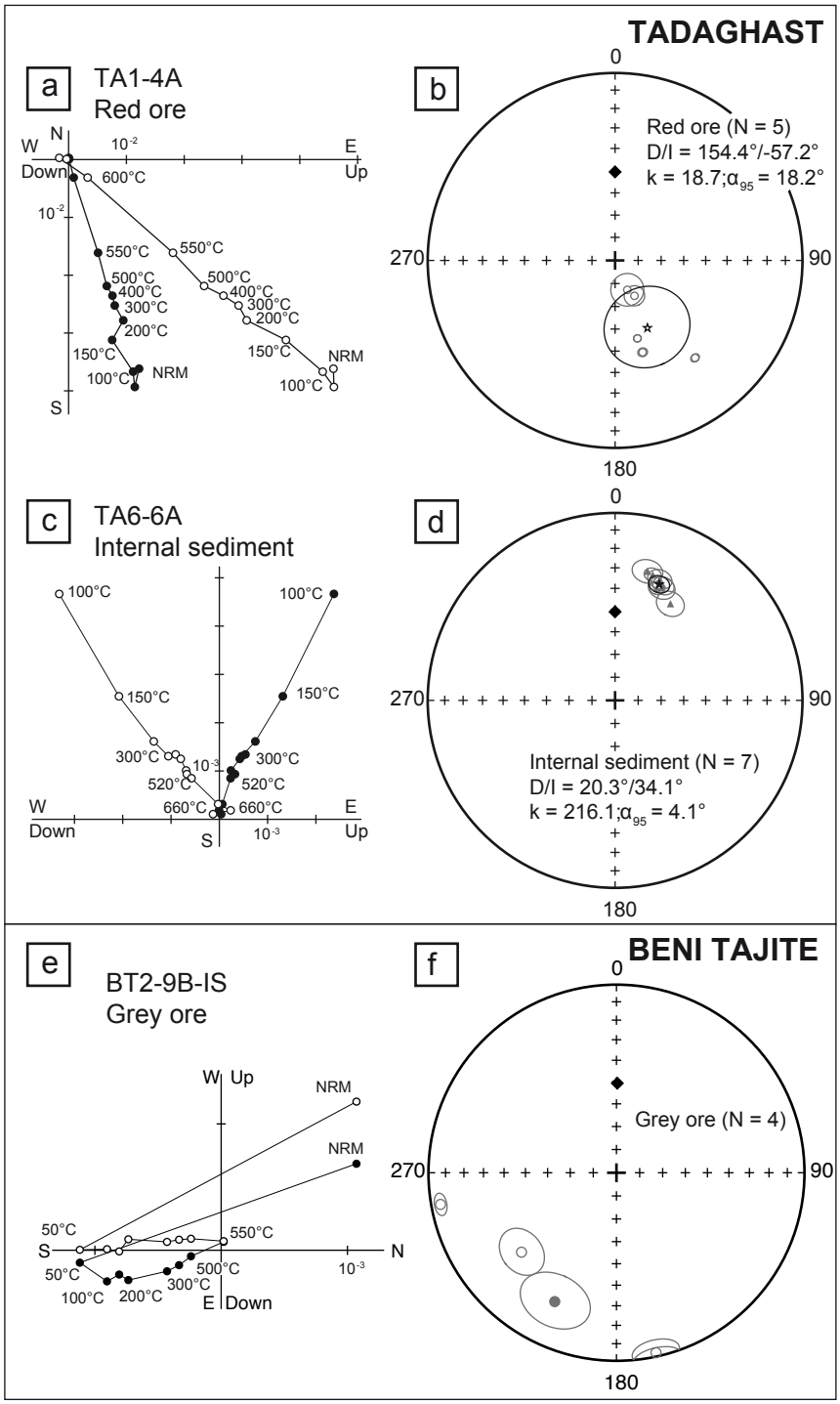

Figure 13

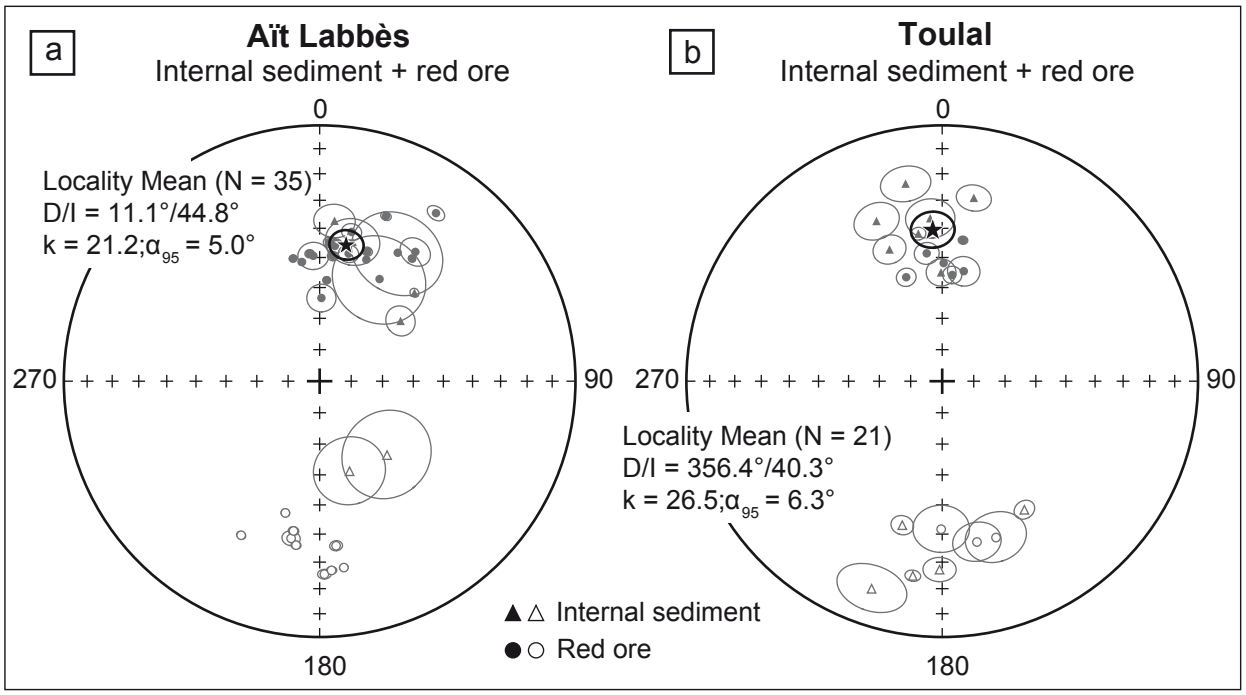
a
Aït Labbès
Internal sediment + red ore
0
90
180
270
Locality Mean (N = 35)
D/I = 11.1°/44.8°
k = 21.2;α95 = 5.0°
b
Toulal
Internal sediment + red ore
0
90
180
270
Locality Mean (N = 21)
D/I = 356.4°/40.3°
k = 26.5;α95 = 6.3°
▲△ Internal sediment
●○ Red ore

Figure 14

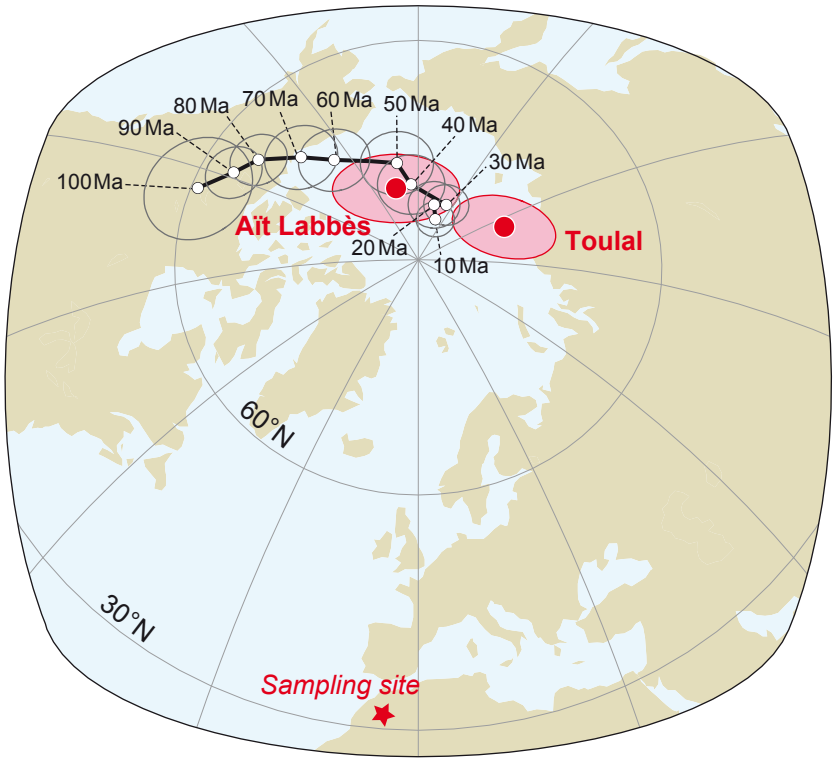
80 Ma
70 Ma
60 Ma
50 Ma
40 Ma
30 Ma
90 Ma
100 Ma
Aït Labbès
20 Ma
10 Ma
Toulal
60°N
30°N
Sampling site

Figure 15

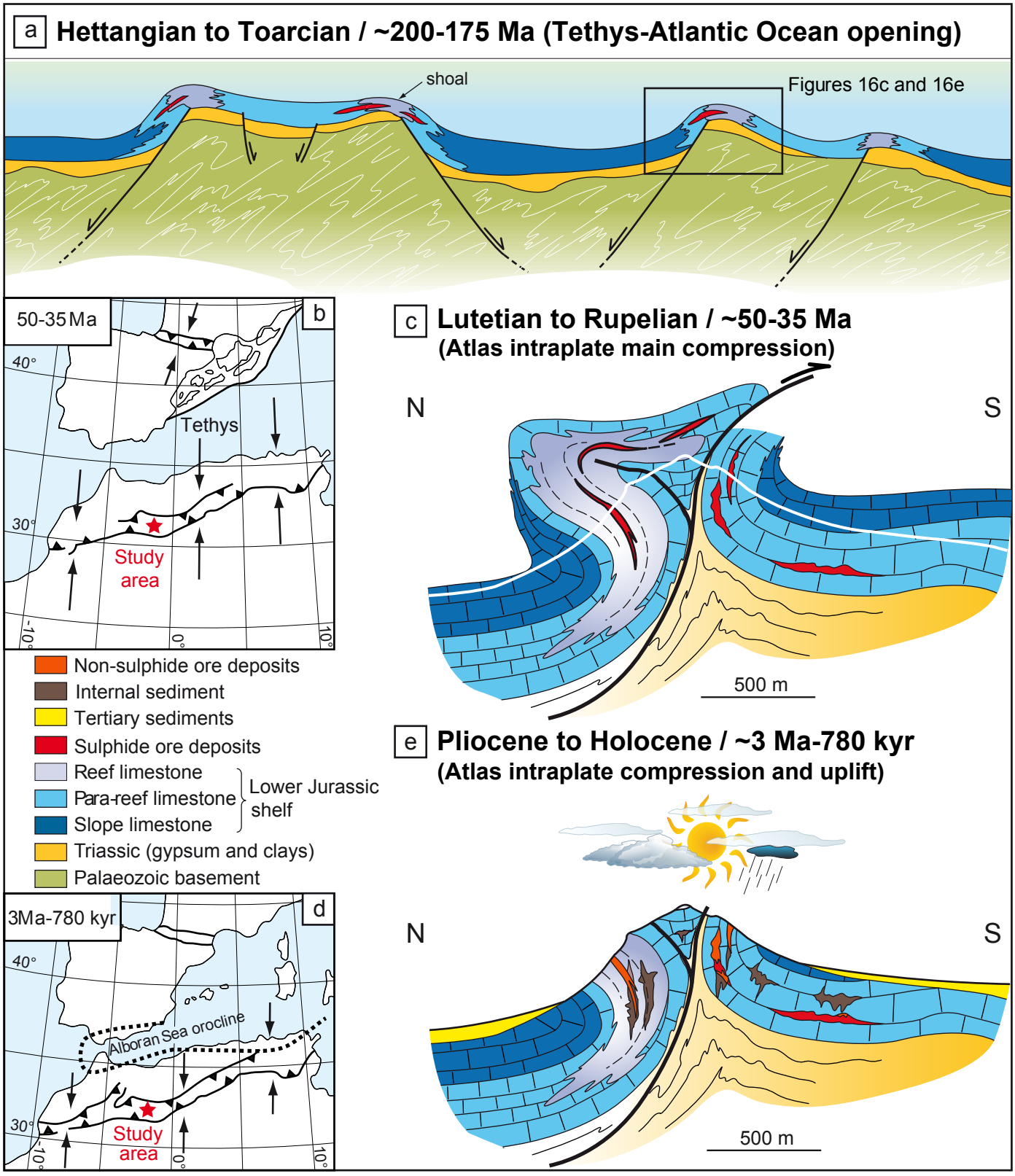
a Hettangian to Toarcian / ~200-175 Ma (Tethys-Atlantic Ocean opening)
shoal
Figures 16c and 16e
50-35 Ma
b
40°
30°
Tethys
Study area
-10°
0°
10°
Non-sulphide ore deposits
Internal sediment
Tertiary sediments
Sulphide ore deposits
Reef limestone
Para-reef limestone
Slope limestone
Lower Jurassic shelf
Triassic (gypsum and clays)
Palaeozoic basement
c Lutetian to Rupelian / ~50-35 Ma
(Atlas intraplate main compression)
N
S
500 m
e Pliocene to Holocene / ~3 Ma-780 kyr
(Atlas intraplate compression and uplift)
N
S
500 m
3Ma-780 kyr
d
40°
30°
Alboran Sea orocline
Study area
-10°
0°
10°

Figure 16

Table 1

Table 1

Deposit	n/N	Km ($x10^{-6}$ SI)	P_J	T	K_1				K_2				K_3			
					D (°)	I (°)	α_{95max}	α_{95min}	D (°)	I (°)	α_{95max}	α_{95min}	D (°)	I (°)	α_{95max}	α_{95min}
Aït Labbès (N32.384°; W04.384°)																
AL1 - Red ore	21/26	13.5	1.001	0.051	232.1	27.1	49.2	20.9	357.0	48.2	49.4	21.5	125.5	29.1	23.1	21.0
AL1 - Host limestone	6/6	30.1	1.015	0.499	329.1	15.7	31.3	11.0	231.4	25.4	31.3	4.7	87.6	59.5	11.6	3.8
AL2 - Red ore	10/18	561.0	1.009	-0.183	317.8	48.9	24.6	17.1	70.4	18.6	21.2	11.0	174.1	35.1	25.2	15.2
AL3 - Internal sediment	16/19	40.1	1.004	-0.059	80.5	4.7	37.9	20.5	350.3	2.6	39.6	20.3	231.9	84.6	25.1	20.6
AL3 - Red ore	6(N)	*no calculation - scattered data*														
Toulal (N32.305°; W03.986°)																
T1 - Internal sediment	30/31	291.0	1.026	0.743	282.0	1.9	68.3	8.3	12.0	0.0	68.3	8.1	102.8	88.1	9.5	8.2
T2+T3 - Red ore	16/22	314.0	1.006	0.301	83.0	3.0	60.7	3.0	173.5	10.4	60.7	16.7	336.8	79.2	18.2	12.0
T1+T2+T3 - Host limestone	9/12	76.9	1.011	0.008	35.0	49.7	28.7	13.0	181.9	35.4	22.6	14.2	284.2	16.7	29.8	14.4
Beni Tajite (N32.302°; W03.451°)																
BT1/BT2 - Grey ore	47/49	49.3	1.035	0.391	310.8	0.1	18.6	9.4	220.8	2.2	48.9	12.7	44.0	87.8	48.4	8.4
Tadaghast (N31.636°; W06.606°)																
TA1 - Red ore	8/10	161.0	1.003	-0.361	276.0	5.8	17.4	10.9	177.0	57.3	37.8	15.0	9.6	32.1	37.3	10.6
TA1 - Host limestone	5/5	6.7	1.029	-0.109	97.7	13.9	28.5	7.8	351.3	48.9	17.2	4.9	198.8	37.8	29.4	12.2
TA2 - Red ore	7/11	180.0	1.002	-0.283	11.6	58.1	20.7	6.3	196.3	31.8	37.4	16.6	105.0	2.1	36.1	6.2
TA2 - Host limestone	3(N)	*no calculation - not enough data*														
TA3 - Internal sediment	21/21	695.0	1.033	0.641	36.8	2.4	11.4	3.7	306.6	5.1	11.4	8.2	152.0	84.4	8.7	4.1

Table 2

Site	n	D [°]	I [°]	MAD [°]
AIT LABBES				
Red ore				
AL1-12	9	34.7	21.2	2.5
AL1-14	9	1.2	63.4	4.5
AL1-1B	8	21.9	31.1	1.5
AL1-21A	4	30.4	51.8	14.4
AL1-4A	9	6.6	44.8	.0
AL1-4A	11	357.1	49.4	4.6
AL1-6A	8	21.0	47.8	.1
AL1-6A	10	12.8	47.6	3.0
AL2-12B	8	31.3	40.9	13.8
AL2-3B	8	178.6	-25.5	1.8
AL2-3B	9	188.2	-35.5	1.4
AL2-4B	10	190.3	-37.6	2.6
AL2-7	9	189.9	-40.3	1.5
AL2-7	10	194.6	-45.8	1.3
AL2-8B	8	37.0	39.8	1.1
AL2-8B	4	36.5	37.2	4.6
AL1-11	11	20.2	45.1	1.5
AL1-13A	10	6.0	49.3	1.6
AL1-13B	9	6.4	45.8	2.5
AL1-15B	9	4.0	57.5	1.2
AL1-5A	10	351.5	51.1	1.1
AL1-5B	10	347.8	49.4	1.2
AL1-6B	9	355.5	48.6	1.4
AL1-7	4	12.1	40.1	2.9
AL2-10A	10	3.9	44.7	1.7
AL2-10B	6	176.4	-26.8	1.4
AL2-2	9	207.0	-32.9	1.3
AL2-3A	6	174.3	-35.6	1.8
AL2-4A	3	172.6	-27.4	1.2
Mean	**N = 29; D/I = 11.1°/42.8°; k = 31.0; a_{95} = 4.9°**			
Internal sediment				
AL3-1A	7	47.0	48.0	1.4
AL3-5B	5	161.6	-59.6	11.1
AL3-6A	8	53.3	57.6	4.7
AL3-6C	4	137.6	-57.9	14.1
AL3-7A	8	5.3	37.1	5.9
AL3-7B	8	13.3	43.3	8.0
Mean	**N = 6; D/I = 11.5°/55.0°; k = 12.5; a_{95} = 19.7°**			

Site	n	D [°]	I [°]	MAD [°]
BENi TAJITE				
Grey ore				
BT1-11A	6	230.1	-34.5	9.8

Site	n	D [°]	I [°]	MAD [°]
TOULAL				
Red ore				
T2-1	15	353.1	48.3	3.7
T2-11	8	8.4	43.6	1.4
T2-13A	7	11.1	53.9	4.9
T2-13B	10	340.9	54.6	3.0
T2-14	4	161.0	-35.6	8.8
T2-14	4	180.4	-41.7	8.2
T2-4	5	.7	51.9	.7
T2-5	2	167.8	-35.9	6.9
T2-7	7	5.4	55.7	2.9
Mean	**N = 9; D/I = 356.0°/47.3°; k = 54.0; a_{95} = 7.1°**			
Internal sediment				
T3-15A	7	349.5	22.5	6.7
T3-3B	9	359.4	55.0	4.5
T3-4A	11	355.8	36.3	7.0
T3-2A	4	338.2	43.8	4.9
T3-4A	10	180.8	-27.2	4.5
T3-5A	8	337.7	32.8	6.5
T3-6B	8	198.8	-15.4	9.1
T1-17	10	9.8	28.1	4.8
T1-6A	10	188.6	-24.1	2.1
T1-7A	8	195.5	-41.2	3.3
T1-8	10	147.4	-40.1	3.1
T1-9	8	350.8	41.2	2.2
Mean	**N = 12; D/I = 356.7°/34.9°; k = 22.4; a_{95} = 9.4°**			

TADAGHAST				
Red ore				
TA1-2A	6	151.3	-72.5	4.4
TA1-2B	8	157.4	-76.2	7.1
TA1-3	7	140.6	-33.2	1.8
TA1-4A	9	163.3	-47.6	2.0
TA1-4B	10	164.0	-54.4	1.6
Mean	**N = 5; D/I = 154.4°/-57.2°; k = 18.7; a_{95} = 18.2°**			
Internal sediment				
TA6-2A	10	29.8	40.3	5.7
TA6-3A	8	20.4	36.4	2.9
TA6-3B	5	16.7	30.7	3.3
TA6-4B	10	20.3	31.7	4.7
TA6-5B	10	22.9	34.0	4.2
TA6-6A	9	22.5	35.3	5.3
TA6-7A	10	14.1	29.7	5.8
Mean	**N = 7; D/I = 20.3°/34.1°; k = 216.1; a_{95} = 4.1°**			